Theoretical study of structural and electronic properties of 2*H*-phase transition metal dichalcogenides

Michele Pisarra [*]
Instituto IMDEA Nanociencia, Calle Faraday 9, 28049, Madrid, Spain
and Departamento de Química, Módulo 13, Universidad Autónoma de Madrid, 28049 Madrid, Spain

Cristina Díaz [†]
Departamento de Química, Módulo 13, Universidad Autónoma de Madrid, 28049 Madrid, Spain;
Condensed Matter Physics Center (IFIMAC), Cantoblanco, 28049 Madrid, Spain;
and Institute for Advanced Research in Chemistry (IAdChem), Universidad Autónoma de Madrid, 28049 Madrid, Spain

Fernando Martín
Instituto IMDEA Nanociencia, Calle Faraday 9, 28049, Madrid, Spain;
Departamento de Química, Módulo 13, Universidad Autónoma de Madrid, 28049 Madrid, Spain;
and Condensed Matter Physics Center (IFIMAC), Cantoblanco, 28049 Madrid, Spain

(Received 7 December 2020; revised 14 April 2021; accepted 15 April 2021; published 13 May 2021)

Computational physics and chemistry are called to play a very important role in the development of new technologies based on two-dimensional (2D) materials, reducing drastically the number of trial and error experiments needed to obtain meaningful advances in the field. Here, we present a thorough theoretical study of the structural and electronic properties of the single-layer, double-layer, and bulk transition metal dichalcogenides MoS_2, $MoSe_2$, $MoTe_2$, WS_2, WSe_2, and WTe_2 in the 2*H* phase, for which only partial experimental information is available. We show that the properties of these systems depend strongly on the density functional theory approach used in the calculations and that inclusion of weak dispersion forces is mandatory for a correct reproduction of the existing experimental data. By using the most accurate functionals, we predict interlayer separations, direct and indirect band gaps, and spin-orbit splittings in those systems for which there is no experimental information available. We also discuss the variation of these properties with the specific chalcogen and transition metal atom.

DOI: 10.1103/PhysRevB.103.195416

I. INTRODUCTION

The isolation of monolayer graphene by micromechanical exfoliation [1] can be considered a milestone in material sciences. Since then, scientists have invested a lot of effort in studying layered materials, whose fundamental 2D units stick together by Van der Waals (VdW) forces. A plethora of stable 2D materials have been proposed [2,3], and more than 150 have been already synthesized [4] since 2004. These materials can be used as building blocks of new Van der Waals heterostructures, whose properties can be tailored by carefully choosing the blocks (and their order) to suit a specific technological demand [5]. This new scenario poses a new challenge for theoreticians: to describe the properties and potential industrial applications of possible 2D materials even before they are synthesized [2]. This scenario renders the research in materials science and engineering much faster and more affordable economically, because it allows for the identification of the promising heterostructures (and discarding the unpromising ones) anticipating the synthesis step, which is, usually, the most arduous and time consuming part of the research. In this context, it is of paramount importance to have a faithful description of the properties of the simulated materials, keeping low the computational costs.

Density functional theory (DFT) within the Kohn and Sham formulation is a reliable and efficient method to treat many electron problems, thus giving access to a computationally affordable modeling strategy to describe many-atoms systems such as large molecules and solids [6]. Being centered on the description of the electrons, DFT results have proved to be very reliable for systems in which the chemical bonding has a prevalent covalent nature, whereas the approximated way in which DFT treats the electron correlation had the shortcoming of making it struggle with systems in which weak dispersion forces have the leading bonding role, due to the improper description of the mutual dynamical charge polarization of the atoms. Several corrections to the original DFT formulation have been introduced to mitigate this problem. Some of them rely on the use of more elaborate, often ad-hoc, exchange-correlation functionals [7–12], while others result from the inclusion of additional terms in the total energy of the system [13–20]. These corrections, usually named van

[*]michele.pisarra@imdea.org
[†]Present address: Departamento de Química Física, Facultad de CC. Químicas, Universidad Complutense de Madrid, 28040 Madrid, Spain.

der Waals (vdW) corrections, have become very relevant in the description of the structural and electronic properties of layered materials. Furthermore, vdW-DFT approaches have already shown a good performance in describing the properties of graphene, graphene-based materials [21–23], and other more complex 2D materials [24–26], although the identification of the most appropriate functional or correction is still a matter of active research. Hence, the study of the performance of these approaches with transition metal dichalcogenides (TMD) is of paramount importance.

Transition metal dichalcogenides are a distinguished class of layered materials. TMDs are constituted by a transition metal (M) and a chalcogen (X), an element of group VI of the periodic table, appearing with an MX_2 stoichiometry. Bulk TMDs are made of triatomic layers, the 2D building blocks, stuck together by dispersion forces, which make them easy to exfoliate to form single and few-layer films. Many transition metals have shown their ability to form TMDs with sulfur, selenium, or tellurium. Depending on the M-X combination, several stable and metastable phases can be observed, each one characterized by specific properties (see, e.g., Refs. [27] and [28] and references therein). Some TMDs are insulators or semiconductors, whereas others are metallic; some of them have the capability to turn superconducting when cooled down to low temperatures or can even exhibit topological phases. For these reasons, single-layer TMDs constitute a very powerful tool kit for material engineering, as they give access to unlimited possibilities for the properties of the heterostructures.

Another very remarkable characteristic of TMDs is the high sensitivity of their properties to stress and strain, which stems from the high sensitivity of their band structure to changes in the crystallographic parameters [29–33]. This phenomenon, which enriches even further the possible technological applications of these materials, turns out to be a real challenge for theoreticians, since a small error in determining the lattice constant can result in huge differences in the predicted band structure and, ultimately, lead to wrong predictions of the physical properties. Furthermore, even for fixed values of the lattice constant, the electronic properties of single-layer TMDs are also very sensitive to the adopted modeling method. The 1T' phase of WTe_2 can be used as a very representative example of this phenomenon. This 2D material was first reported as metallic from calculations making use of the PBE exchange-correlation functional plus spin orbit corrections [34], whereas a later study using a hybrid functional [35] and a similar lattice constant reported a sizable band gap. It is important to mention that high-quality predictions can, in principle, be achieved for single-layer TMDs by using hybrid functionals or post DFT methods, such as the GW one [36]. However such approaches are computationally very costly for systematic studies and, in practice, they are prohibitively expensive when large supercells have to be used to match the periodicity of the material. This is the case, e.g., of multilayer TMDs. For this reason, in this work we will limit ourselves to DFT approaches.

All the above points to the need to carry out, as a preliminary step, systematic studies of the available state-of-the-art DFT methods to identify the most appropriate ones for the description of the structure and electronic properties of TMDs.

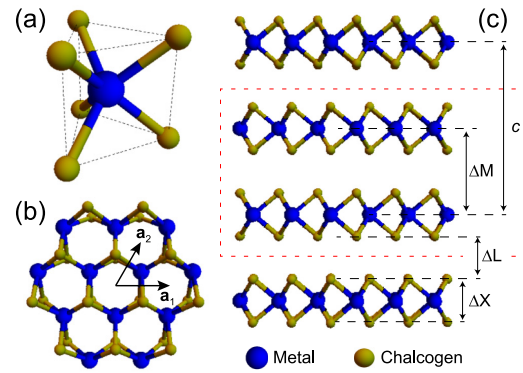

FIG. 1. $2H$ phase of TMDs. (a) The metal atom sits at the center of a right triangular prism, with the chalcogen atoms at the vertices. (b) Top view of the single-layer TMD with a possible choice of the in-plane lattice vectors $\mathbf{a}_1$ and $\mathbf{a}_2$, whose length is the in-plane lattice constant a. (c) Side view of the bulk TMD; the red-dashed line highlights the basic two-layer unit, which is repeated periodically in the vertical direction, with an out-of-plane lattice constant c; several other length definitions used in the text are also highlighted.

In this work, we have performed such a detailed study for the case of the single-layer, double-layer, and bulk TMDs MoS_2, $MoSe_2$, $MoTe_2$, WS_2, WSe_2, and WTe_2 in the $2H$ phase. Our results complement those of Refs. [37–40], which focused on bulk layered materials, by expanding the set of analyzed methods and quantifying their error in predicting the properties of 2D forms (single layer and double layer) of $2H$ TMDs. By using the most accurate functionals, which are identified by direct comparison with the available experimental data, we predict lattice constants, interlayer separations, direct and indirect band gaps, and spin-orbit splittings for those systems where there is no experimental information available. We predict simple trends in the calculated properties and provide numerical data for all considered systems in order to contribute the increasing number of materials science databases created in the last few years (see, e.g., Ref. [41]).

II. THE $2H$ PHASE OF TMDs

We will focus our study on the hexagonal ($2H$) phase of TMDs, in particular, we will analyze materials containing sulfur, selenium, or tellurium as chalcogen, and molibdenum and tungsten as transition metal. As shown in Fig. 1(a), in the $2H$ phase of a TMD the metal atoms are located at the center of a triangular right prism forming six coordination bonds with the chalcogen atoms located in the vertices of the prism. The single-layer $2H$-TMD is made of three atomic layers, organized in two interpenetrated triangular sublattices, which give rise to a graphenelike honeycomb structure [Fig. 1(b)]. For the double layer, two TMD single layers are piled on top of each other in the so-called eclipsed AA' stacking, in which the M atom of the top layer is place directly above the X atom of the bottom layer, and vice versa. The AA' stacking has been reported to be the most stable one for MoS_2, $MoSe_2$, WS_2, and WSe_2 double layers [42]. This double-layer unit is periodically repeated in the out-of-plane direction to obtain the $2H$ phase of bulk TMDs. The out-of-plane lattice vector (of length c) is perpendicular to the TMD plane [Fig. 1(c)].

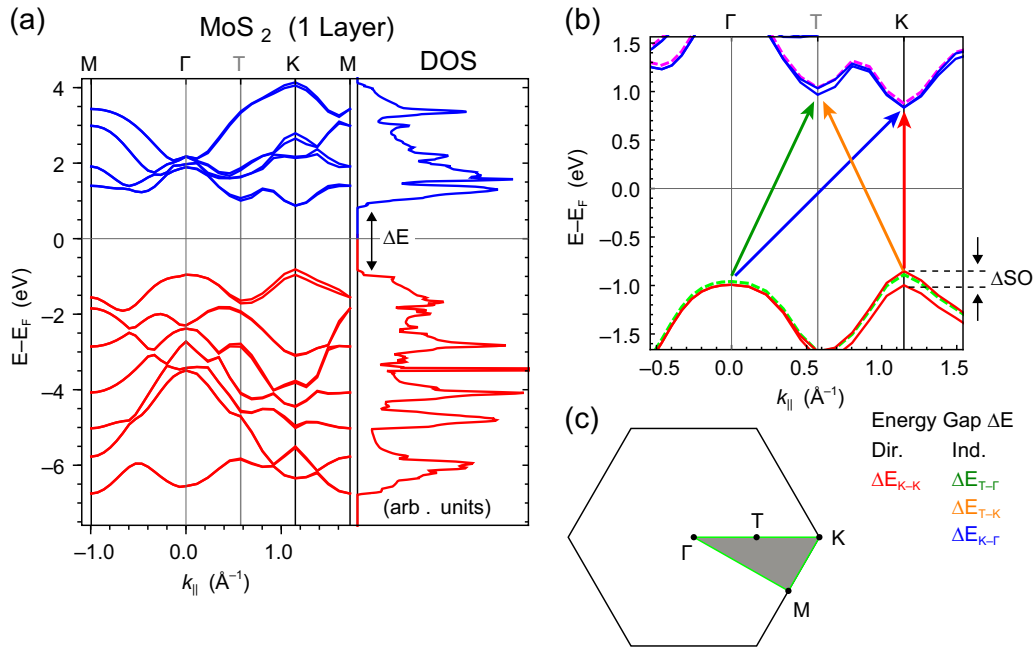

FIG. 2. (a) Band structure and DOS of a single-layer MoS_2 as obtained in this work, using the TS method and including SO corrections (see Sec. III). The displayed energy window includes the highest (in energy) valence bands and the first few lowest conduction bands; in the DOS, the fundamental gap of the system ΔE is highlighted. In (b) a zoom of the energy region close to the Fermi level (located in the middle of the band gap) is given; the dashed lines correspond to the band structure obtained without SO corrections; the arrows define the possible direct and indirect band gaps (legend in the bottom right corner). In (c) the 2D first BZ is shown highlighting (green line) the path used for the band plot and the high symmetry points; the gray shaded region represents the irreducible 2D wedge of the first BZ.

The 2*H* phases of TMDs are semiconducting materials, characterized by a band gap of the order of 1–2 eV [43–47]. As an example, in Fig. 2, we show the band structure and the density of states of a single-layer MoS_2, as obtained in this work by a DFT approach using the PBE functional [48] plus the Tkatchenko-Scheffler (TS) correction [16,17] and including the spin orbit (SO) coupling. In Fig. 2(b), we zoom in on the band structure, focusing on the bands close to the Fermi level to highlight some typical features of this material, which are common to other TMDs in the 2*H* phase. A lot of information can be gained by analyzing the highest-energy valence band (hereafter HVB) and the lowest-energy conduction band (LCB). The HVB has two maxima at the Γ and *K* points of the 2D Brillouin zone (BZ)—these maxima are very close in energy. The LCB has two minima, also very close in energy, at the *K* and *T* points of the BZ. Interestingly, the energy position of these features depends strongly on structural factors such as the lattice constant, the number of TMD layers, the thickness of each TMD layer, or the interlayer distance. This *complex mixture* of minima and maxima gives rise to interesting optical properties for the single- and few-layer TMDs. For example, the single-layer 2*H* MoS_2 presents a direct band gap (at the *K* point), whereas the double layer and the bulk material present an indirect band gap [29,49]. Furthermore, for this material, it has been shown that the size and nature (direct or indirect) of its band gap can be modified by applying external pressure, i.e., by inducing stress and strain to its lattice [29–33].

An interesting feature of 2*H*-TMDs is the lack of inversion symmetry. This fact has a direct effect on the electronic bands, which are spin split due to the spin-orbit (SO) coupling [27]. The splitting reaches its maximum in the HVB at the *K* point—the distance in energy between the spin split states (ΔSO) can be used as a measure of the strength of the SO in the material. Also interesting is the fact that in the band structure of the double-layer TMD the HVB at the *K* point is expected to have degeneration 2, which is lifted by the interlayer interaction. Thus, the splitting of these two electronic levels (before taking into account SO corrections) can be used as a measure of the interaction between the layers in the double-layer TMDs.

III. THEORETICAL METHODS

All the calculations have been carried out using DFT within the PAW formalism [50], as implemented in the VASP code [51–53]. We have adopted a 400 eV energy cutoff for the plane-waves basis, using a total energy threshold of 10^{-6} eV for the self-consistent field calculations. The reciprocal space sampling was carried out using an unshifted $18 \times 18 \times 1$ Monkhorst-Pack grid [54], for slab calculations, and $18 \times 18 \times 7$ for bulk calculations, which, taking advantage of the symmetry operations, resulted in 37 and 148 *k* points, respectively, in the irreducible wedge of the BZ. In all slab calculations, we have adopted an interslab distance of at least 20 Å to ensure negligible influences between the system replicas. All the geometry optimizations were carried out until the maximum force acting on the atoms was less than 0.005 eV/Å. For the optimized structures, we have run an additional single-point energy calculation including the SO correction to obtain the band structure and the density of states (DOS). In such runs, the lattice symmetry was switched off and the full

BZ was sampled with a total of 324 and 2268 k points in slab and bulk calculations, respectively.

Several choices have been adopted for the exchange and correlation energies. We have carried out calculations without including vdW corrections using the local density approximation (LDA) exchange-correlation functional as parametrized by Ceperley and Adler [55], and the generalized gradient approximation (GGA) exchange-correlation functional [56] in the PBE parametrization [48]. To incorporate vdW corrections to the PBE functional, we have carried out calculations using the empirical Grimme D2 correction [13] (D2), the Grimme D3 correction, with [15] (D3-BJ) and without [14] (D3) Becke-Johnson damping, the original Tkatchenko-Scheffler correction [16,17] (TS), the Tkatchenko-Scheffler method with iterative partitioning of the Hirshfeld charges [18] (TS-iter), and the exchange-hole based correction of Steinmann and Corminboeuf [19,20] (dDsC). We have also used several nonlocal exchange-correlation functionals designed to explicitly include the effect of weak dispersion forces [7], in particular the DF functional [8], developed by Dion *et al.* [9], and subsequent modifications, specifically the DF2 functional of Langreth and Lundqvist [10] and the rev-DF2 functional by Hamada [11]. We have also used the three available opt-vdW functionals [57], namely opt-PBE-vdW, opt-B88-vdW, and opt-B86b-vdW (shortened as optPBE, optB88, and optB86b, respectively) and the SCAN+rVV10 (shortened as SCAN) functional by Peng *et al.* [12].

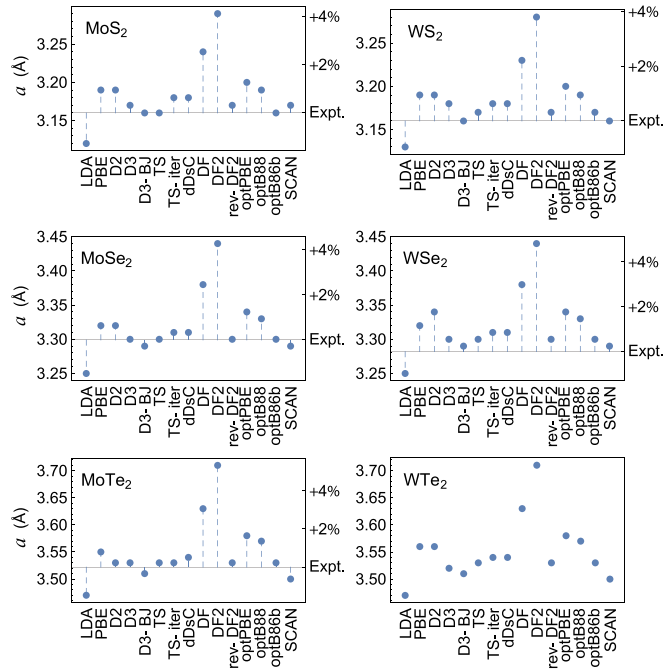

FIG. 3. Comparison of the in-plane lattice constant a resulting from the different methods used in this work with the available experimental values (Expt.) [44,59–61] for the six single-layer TMDs.

IV. RESULTS

A. Single-layer 2*H* TMDs

1. Structural parameters

We have computed in-plane lattice constants of single-layer TMDs, in the 2H phase, using the DFT approaches described in Sec. III. To accomplish this task, given a method, for each material, we have run several geometry optimizations, in which the coordinates of all the atoms were left free to relax whereas the in-plane lattice constant value was chosen in a relevant length range. Doing so, we obtain the total energy of the optimized structure as a function of the lattice constant, which can be fitted using a model function [58] to obtain the best value for the in-plane lattice constant and the in-plane Bulk modulus (B_{2D}). The values for the lattice constant, the 2D bulk modulus, and the band gap obtained for the six single-layer TMDs considered in this work are collected in Tables I–VI (see Appendix C 1). In these tables, we also provide other relevant computed quantities and the experimental values when available. Figures give an overview of these results.

In Fig. 3, we compare with the experiments the numerical values of the optimized lattice constants resulting from the different methods. Since the 2H phase is not the equilibrium configuration of WTe_2, there are no experimental values available for this system. One can see that the different methods have a similar *performance* for the six single-layer TMDs. A closer look at the plots reveals that the LDA functional systematically underestimates the lattice constant, which is not surprising due to the well-known overbinding nature of the LDA functional. The PBE functional gives reasonably good results, even though it slightly overestimates the experimental values by roughly 1% on average. Both the LDA and the PBE predictions are in fairly good agreement with the ones reported in previous theoretical works (see, e.g., Refs. [62] and [36]). The discrepancy between PBE and experimental

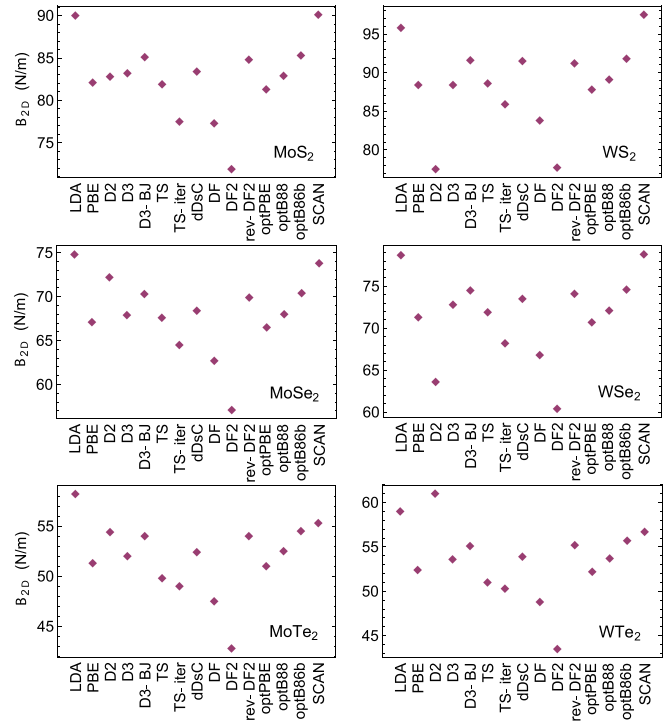

FIG. 4. 2D bulk modulus (B_{2D}) for the six single-layer TMDs.

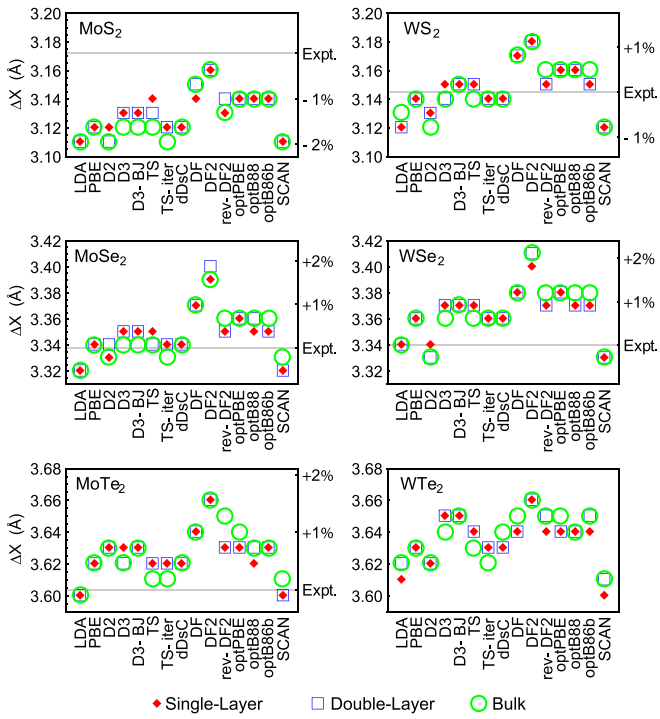

FIG. 5. Comparison of the layer thickness ΔX resulting from the different methods used in this work as obtained for the single-layer (red diamonds), double-layer (blue hollow squares), and bulk (green hollow circles) for the 2*H* TMDs. In all the subfigures the available experimental values (Expt.) [44,59,61] for the single layer are reported for comparison.

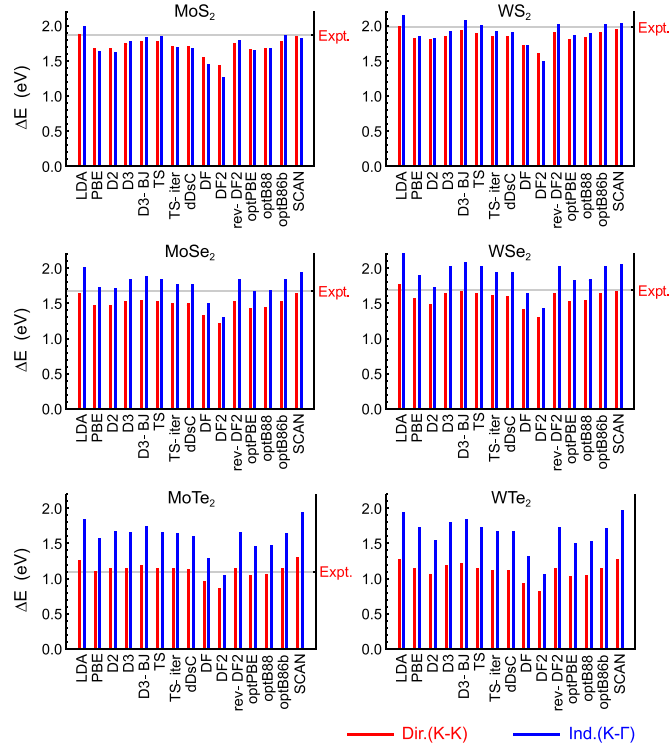

FIG. 6. Direct band gaps at the *K* point (red bars) and indirect band gap between the *K* and Γ points (blue bars), as obtained without including the SO coupling; in each panel the horizontal grid line marks the position of the experimental value of the direct band gap [46,67–71], when available.

values is, in general, mitigated by applying a vdW correction method, among which we single out the Grimme D3 methods and the Tkatchenko-Scheffler corrections as the ones that tend to predict most accurately the lattice constants of the TMDs studied here. As for the nonlocal functionals, the DF and DF2 methods systematically overestimate the lattice constants, being the two methods that show the largest distance from the experimental values. Much better results are obtained with the rev-DF2 functional, whereas among the "opt" functionals, the best results are obtained with the optB86b-vdW functional. It is important to mention that, for the LDA, PBE, PBE+correction, and SCAN methods, the inclusion of the SO coupling in the optimization of the lattice constants does not lead to any appreciable change, while for the nonlocal functionals used in this work the resulting values are in worse agreement with the experiments (see Appendix B).

In Fig. 4, we report the values of the 2D bulk modulus (given in N/m), calculated as described in Appendix A, for all methods considered in this work. From this figure, we observe that, regardless of the applied method, the bulk moduli obtained in this work underestimate by roughly a factor 2 the experimental values for MoS_2 (171 N/m) and WS_2 (177 N/m), the only ones available in the literature [63]. This underestimation is due to the phenomenological model function used to obtain the bulk modulus, which is designed to describe 3D bulk materials (see Appendix A). Much more accurate modeling is needed to describe the elastic properties of 2D materials [64]. Furthermore, it is well known that DFT approaches fail to provide accurate values for the elastic properties of semiconductors [65]. Nonetheless, the comparison of the bulk moduli provided in Fig. 4 is very informative, because this quantity gives information on the energy needed to induce a change in the structural parameters of the material. In practice, it influences the choice of the *final* in-plane lattice constant of an interface made of different materials when lattice constant matching is required, which is the usual situation in periodic DFT approaches. Focusing on the results, we observe similar plots for the different materials, with the exception of the D2 method that shows an *erratic behavior*, proving that the different approaches predict similar trends for the different materials. In particular, we observe that the LDA and the SCAN functionals tend to yield the highest values of the bulk modulus, whereas the DF and DF2 functionals yield the lowest values.

Another important quantity is the layer thickness ΔX, defined as the vertical distance between the chalcogen atoms of each single layer [see Fig. 1(c)], since it determines, with the in-plane lattice constant, the critical interatomic distances. The values of ΔX for the single layer, as calculated with the different methods, are reported in Fig. 5 (red diamonds). In this case, in contrast with the in-plane lattice constant and the bulk modulus, the results of the different approaches generally agree with each other, within a maximum spread of $\sim$1.5%. Furthermore, looking at the experimental values for this quantity, we find that all the approaches tend to give a reasonably good prediction, since the maximum relative difference

between the experimental and calculated values is never higher than 2%. Once again, the DF and DF2 approaches tend to give the highest values of ΔX, whereas LDA and SCAN give the lowest ones.

2. Electronic properties

In Fig. 6, we show the calculated direct (at the K point) and indirect (between the Γ and K points) band gaps, and we compare them with the experimental values of the direct band gap, when available. In general, all methods tend to slightly underestimate the band gaps for all the TMDs studied here, with the exception of $MoTe_2$, for which most of the methods seem to predict an accurate value. The LDA functional tends to give the highest values for both direct and indirect gaps for all the materials, whereas the DF and DF2 methods give the lowest values. We point out that the relative difference between the highest values of the gaps, predicted by the LDA functional, and the lowest ones, predicted by the DF2 functional, is as high as 25%. Another important result is related to the relative values of the direct and indirect gaps. From Fig. 6, we can see that, for all the materials, the ratio is not constant and depends strongly on the adopted method. This fact is especially relevant in MoS_2 and WS_2, for which, in some cases, the predicted value of the indirect band gap is lower than the direct one. This result reveals that different choices for the modeling of the van der Waals interaction may cause a different prediction of the general physical properties of the material. In fact, some approaches predict that the TMDs of the form XS_2 are indirect band-gap semiconductors, instead of direct band-gap semiconductors. It is important to point out that including the SO coupling in the band structure calculations results in an overall reduction of all the gaps, with the direct gaps being mostly reduced, as a consequence of the large band splitting in the HVB at the K point. We can then observe that the inclusion of the SO coupling results in a worse numerical prediction of the band gap, emphasizing that more sophisticated theories are needed for a correct description of this quantity. On the other hand, the SO coupling restores [66] the *correct* physical nature of the single-layer S-containing TMDs, as it predict them to be direct gap semiconductors.

At this point, it is worth considering the relative spread of the predicted data for the three quantities analyzed so far. In the case of the lattice constant, we observe that in the worst case (DF2 functional), the discrepancy is of the order of 4–5%, whereas, in general, the computed values show a relative spread around the experimental value of the order of 1–2%—such discrepancies, usually, are *acceptable* in DFT calculations. For the bulk modulus, we have found a spread of $\pm 15\%$ around the numerical average, hence the relative spread of the predicted values for the bulk modulus is much higher than for the lattice constant. This wider range could lead to serious errors when interfaces are modeled. Finally, a similar window of predicted values is also observed for the band gap, in which we witness the interplay of two effects. On one hand, the different exchange-correlation functionals predict different band structures, which result in different band gaps. On the other hand, the different functionals predict different values of the lattice constant, which, due to an inherent property of the

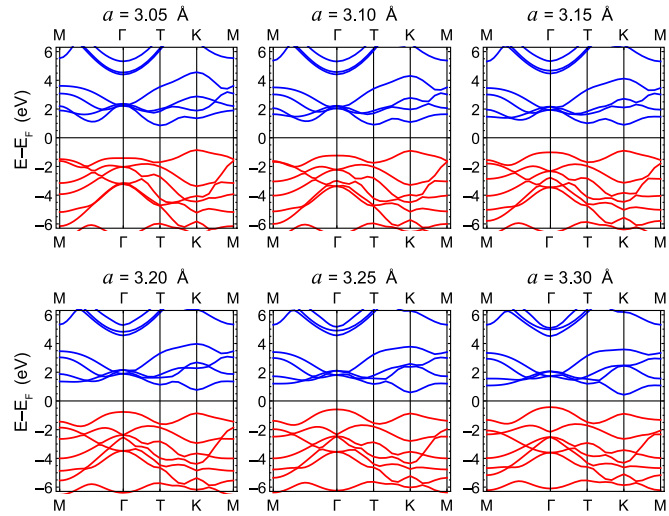

FIG. 7. Band structure of MoS_2 along the MΓKM BZ path, as calculated by the TS method, without taking into account the SO coupling, for eight different values of the lattice constant a in the 3.05–3.30 Å range.

$2H$ phases of the TMDs, gives rise to strong modifications of the band structure and ultimately to different values of the band gaps. As an example of this phenomenon, in Fig. 7 we show the calculated band structure for MoS_2, using the TS method, for different values of the lattice constant. In this figure, we observe noticeable variations of the dispersion of different bands, even though the lattice constant was chosen in a interval within a 5% distance from the experimental value. Furthermore, the HVB and LCB are the most affected bands, evidencing that different values of the lattice constant results in noticeable differences in the band gap values. Finally, we observe that the band modifications are not rigid shifts, hence in addition to the variation of the band gap different choices of the lattice constant change also the nature of MoS_2, from a direct gap semiconductor to an indirect gap semiconductor.

The possibility of changing the value of the band gap, and the band gap nature, from direct to indirect, in MoS_2, by inducing structural deformations was already predicted [29,30] and subsequently observed experimentally [31–33]. How this fact affects the prediction of the band gap obtained by different exchange correlation functionals is further investigated in Fig. 8, in which we plot the direct and indirect band gaps as a function of the lattice constant for MoS_2. In this figure, we display results for (i) LDA, which underestimate the lattice constant; (ii) DF2, which highly overestimate it; (iii) PBE, which slightly overestimate it; and (iv) TS, which predict the experimental value. The four plots reveal a complex behavior of the direct and the indirect band gaps when the lattice constant increases. Both the direct gap, ΔE_{K-K} and the indirect gaps, $\Delta E_{K-\Gamma}$ and $\Delta E_{T-\Gamma}$, decrease with a, even though they exhibit different decreasing rates. The decrease of $\Delta E_{K-\Gamma}$ is the fastest, whereas the decrease of $\Delta E_{T-\Gamma}$ is the slowest. On the contrary, the indirect band gap ΔE_{T-K} increases with a. As a consequence, the indirect band gap ΔE_{T-K} has the lowest value for small values of a. We can also observe that, in a small range of values of the lattice constant a, the material behaves as a direct band gap semiconductor,

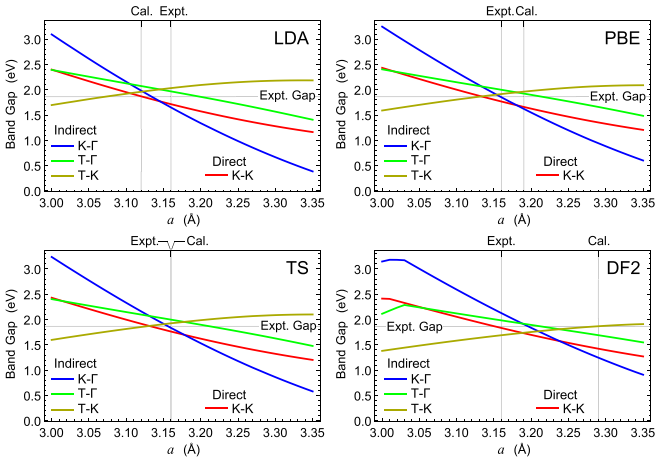

FIG. 8. Direct and indirect band gaps as a function of the lattice constant, for four different methods analyzed in this work. Three different indirect band gaps are considered. In each panel, the horizontal grid line marks the experimental value of the direct band gap, whereas the vertical grid lines mark the experimental (Expt.) and the calculated (Cal.) values of the lattice constant, as predicted by each method.

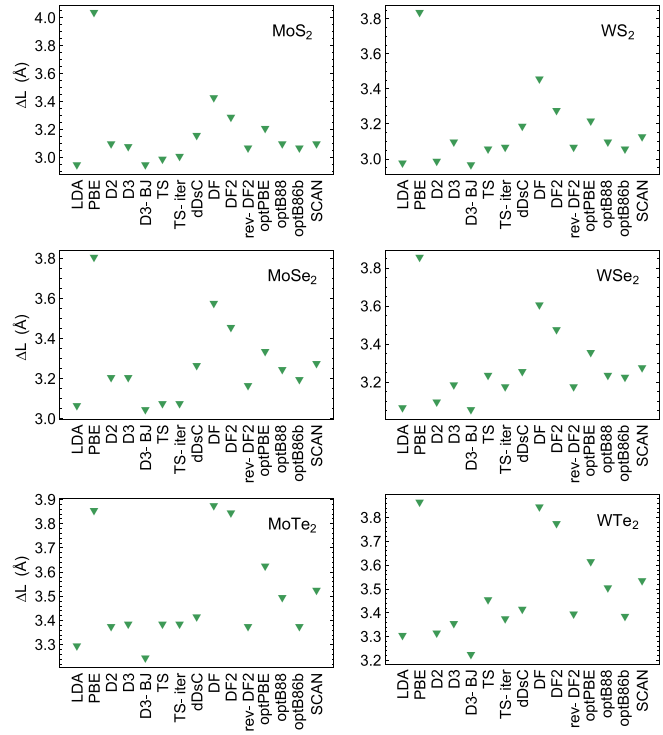

FIG. 9. Interlayer distance (ΔL) for the double-layer TMDs as obtained with the different methods.

with the gap at K. Finally, for large values of a, the indirect band gap $\Delta E_{K-\Gamma}$ is the lowest gap. The different dependence (increasing or decreasing, with a different rate of change) of each band gap on the value of the lattice constant appears to be independent on the modeling method. This fact could be correlated to the different orbital composition of the wave function of each band at the different points in the BZ [72]. Nevertheless, a comparative look at the four plots in Fig. 8 shows that the different methods lead to overall different predictions. For instance, depending on the method, we find that the different functions cross at different values of a. In summary, regardless of the applied functional or correction method, we see that the value of the lattice constant plays a key role in determining the value of the band gap and the direct-band-gap or indirect-band-gap semiconductor nature of the material.

B. Double-layer 2*H* TMDs

The very important feature of vdW correction methods or vdW functionals is their capability to describe chemical binding of dispersive nature. Therefore, such methods should be more appropriate to investigate multilayer TMDs. To investigate this issue, we have first studied a double layer of each of the analyzed TMDs, which can be considered the simplest system for which one can test the interlayer interaction of single-layer TMDs. To set up the double-layer calculations, we use the unit cell as described in Sec. II and fix the in-plane lattice constant to the optimized values as obtained in the single-layer calculation (hence we use different values of a for the different methods). In test calculations we verified that the optimized in-plane lattice constant for the double layer differs by a maximum of 0.01 Å from the value of the single layer (see Appendix D). Given these initial conditions, we optimize the position of all the atoms.

The relevant quantities are collected in Tables VII–XII (Appendix C 2). A visual representation of the interlayer spacing (ΔL) is given in Fig. 9. We can identify some trends in the performance of the different approaches that are common to all TMDs. For all TMDs, the PBE functional predicts the highest value of the interlayer separation ΔL. This result highlights the well-known fact that the PBE functional is not appropriate to describe a situation in which the interaction has a leading vdW nature. The DF, DF2, and optPBE-vdW functionals also predict high values of the interlayer separation. On the other hand, the LDA and D3-BJ yield the lowest values. Finally, it is worth pointing out that even if we discard the predictions of the PBE functional, we, once again, find a pretty wide range of predicted data, with the relative difference between the highest predicted values and the lowest ones of the order of 15–20%. This last observation is in striking contrast with what happens to the thickness of each layer, ΔX, in the double layer (see Fig. 5). Indeed, we find that all the methods tend to give a value of ΔX within a $\sim$2% of relative spread. Furthermore, regardless of the modeling method, the values for the double layers are very similar to those for the single layers. Hence, the discrepancies between the methods is much stronger in the quantities related to interlayer interactions.

Turning our attention to the electronic properties of the double layers (see Fig. 10), we find that, in general, all the methods predict the double layer TMDs to be indirect gap semiconductors, in agreement with what it is reported in the available experimental studies [46,67,71]. Interestingly, there are a few notable exceptions, namely the PBE and DF functionals, which predict a direct fundamental gap for some of the materials. In general, we witness once again a correlation

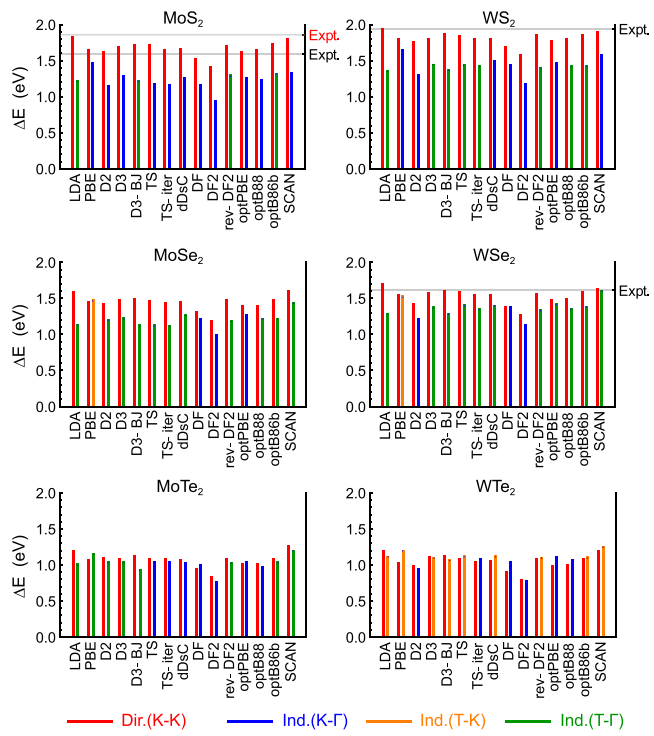

FIG. 10. Direct band gaps at the K point (red bars) and the minimum indirect band gap K-Γ (blue bars), T-K (orange bars), and T-Γ (green bars) as obtained without including the SO coupling for the double-layer TMDs. In each panel the horizontal grid lines mark the position of the experimental value of the fundamental (black) or direct (red) band gaps [46,67,71] when available.

between the structural properties and the electronic properties, observing that the methods that predict a large ΔL tend to predict close values for the direct and indirect band gaps, with some cases in which the direct band gap is lower than the indirect one. Figure 10, in which we also distinguished the different indirect band gaps, provides a clear evidence of the sensitivity of HVB energies at the K and Γ points, which depend strongly on the interlayer interaction. A similar argument holds for the minima in the LCB, which are located at the K and T points of the BZ. Hence, a slight variation in the arrangement of the atoms, due to the chosen DFT approach, results in a shift of the band features and of the BZ points responsible for the minimum indirect band gap. Finally, from Fig. 10, we observe that all the employed DFT approaches underestimate the gap with respect to the experimental values for MoS_2, WS_2, and WSe_2, the only materials for which experimental data are available.

C. Bulk 2*H* TMDs

To complete our study, we have assessed the performance of the different vdW approaches to describe the properties of bulk 2H-TMDs. To do so, we adopted the calculated in-plane lattice constant a of the single-layer material. As in the case of the double layer, test calculations (Appendix D) indicate that this procedure entails a maximum 0.01 Å difference between the adopted and the optimized in-plane lattice constant of the bulk material. In the geometry optimizations, we relaxed

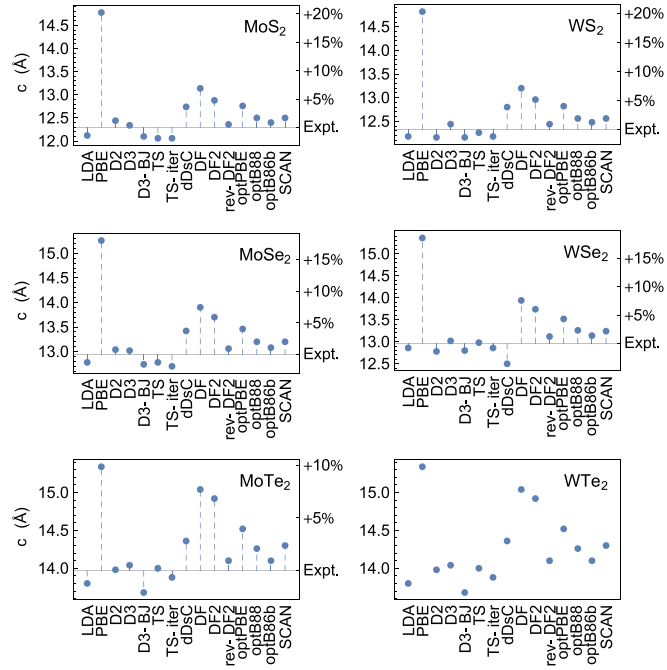

FIG. 11. Out-of-plane lattice constant c for the bulk TMDs, compared to the available experimental values (Expt.) [59–61], as obtained with the different methods used in this work.

the positions of all atoms in the 3D minimal unit cell while changing the value of the out-of-plane lattice constant c in a suitable length interval. In this way, we obtained the total energy as a function of c, which was then fitted with a model function to get the optimal c and the *out-of-plane bulk modulus* B_z. We have also calculated the electronic properties for the optimized values of c with and without SO coupling. The relevant quantities for the six TMDs and all the adopted methods are reported in Tables XIII–XVIII (see Appendix C 3). The results for out-of-plane lattice constants c, the direct ΔE_{Dir}, and the fundamental ΔE_{Fund} band gaps are shown in Fig. 11 and Fig. 12, respectively.

Figure 11 shows that the quality of the predictions of the different methods for the out-of-plane lattice constant c is similar for the different materials. As in the case of double-layer TMDs, the PBE functional overestimates c by a large amount, whereas all the PBE+vdW correction approaches (excluding the dDsC) lead to a more reasonable agreement with the experimental value. The LDA functional tends to underestimate the experimental lattice constant even though, in general, it gives values in line with the PBE+correction schemes. As of the nonlocal functionals, the DF and DF2 tend to overestimate by large amounts the experimental values, whereas the ref-DF2 functional does a much better job. Finally, the opt-vdW functionals tend to overestimate c, even though the opt-B86b-vdW functional gives results very close to the experimental values. It is important to point out that, since the quantity c has a value larger than 10 Å, a relatively small (1%) discrepancy from the experimental values entails an error of ∼0.15 Å, which is a significant amount. Regarding the intralayer features, on the other hand, we observe that the predicted values of ΔX for the bulk materials (green circles in Fig. 5) show a much smaller relative spread ($\lesssim 2\%$) and

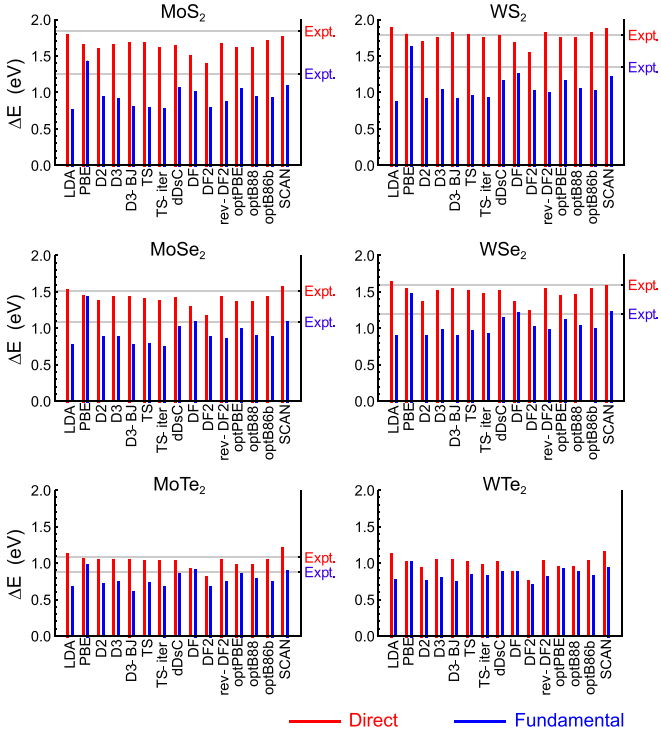

FIG. 12. Direct band gap (red bars) and fundamental band gap (blue bars) as obtained without including the SO coupling for the bulk TMDs. In each panel the horizontal grid lines mark the position of the experimental values for both band gaps (Expt.) [43–47] when available.

they do not differ significantly from the values obtained for the single layer and the double layer.

As for the electronic properties (see Fig. 12), we observe that all the functionals tend to slightly underestimate both the direct and the fundamental band gaps. We further observe that the functionals that tend to overestimate the value of c lead to the highest values for the gap and to the best agreement with the experimental values. Since a large value of c means small interlayer interactions (i.e., we are approaching the single-layer case), we conclude that the better agreement in these cases is due to a cancellation of errors. Finally, we observe that including the spin-orbit coupling leads to a reduction of all the values of the band gaps, similar to what we have found in the single-layer case.

V. DISCUSSION

From the assessment of the different DFT approaches presented in the previous sections, we can select the "best" methods and use them to find trends and propose realistic values of specific physical quantities that are hardly measured in experiments or for which the experimental record is not complete yet. We base our choice on the performance of each method on reproducing the in-plane lattice constant of the single-layer and the out-of-plane lattice constant of the bulk materials, for which complete experimental records exist. Going back to Fig. 3 and Fig. 11, we can recognize D3, D3-BJ, TS, TSiter, rev-DF2, and optB86b as the approaches that more closely reproduce the experimental measurements.

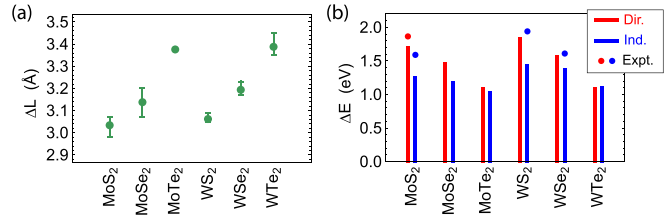

FIG. 13. (a) Best prediction of the interlayer distance ΔL for the double-layer TMD films. The points represent the numerical average of the values obtained from the D3, D3-BJ, TS, TSiter, rev-DF2, and optB86b approaches, whereas the error bars are obtained from the minimum and the maximum values resulting from those methods. (b) Comparison of the band gaps of the double-layer TMD films. The vertical bars are the best predictions for the direct (red) and indirect (blue) band gaps, and the points represent the available experimental points with the same color convention. The same set of methods as in (a) was used to calculate the best prediction.

Hence, we can get best predictions for physical quantities (for which no experimental measurements are available) by averaging the calculated values obtained by these methods. In Fig. 13, we carry out such an analysis for double-layer TMD films, focusing, in particular, on the interlayer distance ΔL [Fig. 13(a)] and the value of the band gap [Fig. 13(b)]. It is important to mention that the $2H$ phases of WTe_2 (single-layer, double-layer, or bulk) have not been observed yet in any experiment. However we provide the prediction data also for this material because it is not possible to exclude, *a priori*, that such systems will be synthesized in the future.

Figure 13(a) shows that the interlayer separation ΔL is almost independent on the transition metal. We only observe a faint increase of ΔL when Mo atoms are replaced by W atoms. On the other hand, a strong variation of ΔL with the chalcogen is observed, with ΔL increasing with the atomic number of the chalcogen. The relative difference in ΔL between MTe_2 and MS_2 TMDs is of the order of 30%. Interestingly, similar trends are observed in the values of the in-plane lattice constant in the single-layer (see Fig. 3) and in the out-of-plane lattice constant in the bulk materials (Fig. 13).

Turning our attention to Fig. 13(b), we can observe that, as already pointed out, the predicted band gaps underestimate the experimental values. Nevertheless, in Fig. 13(b) we can recognize several interesting trends. First of all, both band gaps increase slightly when the Mo is replaced by W. On the other hand, we observe that both the direct and the indirect gaps decrease when the atomic number of the chalcogen atom increases. Moreover, we observe that the rate of variation of the direct gap is much faster than the one of the indirect gap. Finally, the double-layer TMDs containing Te are predicted to have very similar values for the direct and the indirect band gaps.

We conclude our study by analyzing the energy splitting due to the SO coupling in the HVB at the K point of the BZ, indicated as ΔSO in Fig. 2. As already pointed out, in the $2H$ TMDs, ΔSO can be considered as a measure of the *strength* of the spin-orbit coupling, which is one of the key factors in the emergence of nontrivial topological phases in TMDs (see, e.g., Refs. [27] or [35]). In Fig. 14(a), we

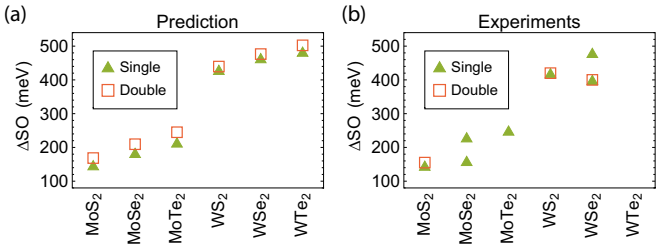

FIG. 14. (a) Best predictions of ΔSO for the single- and double-layer TMDs. The predictions are obtained by averaging the values calculated with the D3, D3-BJ, TS, TSiter, rev-DF2, and optB86b approaches. (b) Experimental values of ΔSO for the single [67–71] and double [46,71] layer TMDs.

report the best prediction of ΔSO for the single-layer and the double-layer TMDs analyzed in this work. Starting from the dataset of the single layer, we can observe that, given a transition metal, ΔSO increases slightly with the atomic number of the chalcogen atom. Furthermore, as expected, by replacing Mo by W, a strong increase in ΔSO is observed due to the larger atomic weight of the metal. The good agreement between our predictions and the experimental data for the single-layer TMDs proves that our predictions for the double-layer systems [Fig. 14(a)], for which the experimental set is not complete, are accurate. In particular, one can see that ΔSO for the double-layer TMDs follows the same trend as for the single-layer TMDs. We finally conclude that, for a given TMD, the value of ΔSO for the double-layer case is slightly higher than that for the single-layer case. This is the consequence of the interlayer interaction in the double-layer system, which further splits the HVB states and generates, in principle, a four-peak fine structure (in the single layer is a double peak), which extends over a wider energy window.

VI. CONCLUSIONS

In summary, our work shows that a proper choice of the DFT approach is crucial to obtain a reasonable description of the structural and electronic properties of TMDs. We have found that even small differences in specific structural parameters, like the lattice constant, lead to large differences in the predicted electronic properties of single and few-layer TMDs, due to the intrinsic sensitivity of these materials to structural deformations. Our results are particularly relevant for the modeling of heterostructure containing TMDs in the hexagonal ($2H$) phase. Identifying a calculation method that is capable of predicting the lattice constant of a building block material in a heterostructure is a mandatory preliminary step, because the lattice constants of the constituent materials (and their stiffness) dictate the choice of the periodicity and the method of matching between the different 2D building block of the heterostructure.

More specifically, we have shown that, as expected, the very popular PBE functional is not able to appropriately describe interlayer interactions in double-layer and bulk TMDs and can also lead to non-negligible inaccuracies in the description of single-layer TMDs. Hence a PBE+correction or an ad-hoc vdW functional is needed to study interfaces made of TMDs. But not all the vdW methods are equivalent. Our results indicate that D2 and dDsC approaches should be avoided for this particular kind of systems, whereas either the Grimme D3 or the Tkatchenko-Sheffler corrections (in both variations analyzed here) yield reasonable results. We have also found good agreement with the experimental measurements with the rev-DF2 and the optB86b functionals. The other nonlocal exchange-correlation functionals analyzed in this work lead, in general, to significant discrepancies when compared to the experimental values. In particular, DF and DF2 methods lead to important discrepancies with experimental values and should be avoided for the TMDs analyzed in this work.

By using the results of the *best* methods, we have proposed best predictions of some quantities for the simplest interface that can be created out of the single-layer TMDs, namely double-layer films. Specifically, we have proposed values for the interlayer separation, for which no experimental record exists. This interlayer separation follows the same trend as the in-plane lattice constant in single-layer TMDs and the out-of-plane lattice constant in bulk TMDs. We have also found that increasing the atomic number of the chalcogen in double-layer $2H$ TMDs decreases the band gap. Moreover, we found that the direct and indirect band gaps are comparable in double-layer $MoTe_2$ and WTe_2. Finally, we have shown that the HVB splitting in double-layer TMDs due to spin-orbit coupling (ΔSO) for which the experimental record is rather poor, follows the same trend as that observed in the single-layer systems. We hope that the results presented in this paper will help to fill the gap in our knowledge of few-layer TMDs, for which experimental information is more difficult to extract than for the single-layer and bulk TMDs.

ACKNOWLEDGMENTS

Work supported by the MICINN projects PID2019-105458RB-I00 and PID2019-106732GB-I00, 'Severo Ochoa' Programme for Centers of Excellence in R&D (MINECO Grant No. SEV-2016-0686), and 'María de Maeztu' Programme for Units of Excellence in R&D (MICINN Grant No. CEX2018-000805-M). C.D. acknowledges the Ramón y Cajal program of the MINECO. We acknowledge the generous allocation of computer time by the Red Española de Supercomputación at the CESGA and Mare Nostrum computer centers and by the Centro de Computación Científica at the Universidad Autónoma de Madrid (CCC- UAM).

APPENDIX A: FITTING PROCEDURE

In order to get the lattice constant and bulk modulus of a given material, we have calculated the total energy (E) by means of DFT calculations for different values of the volume (V) and fitted it to the Birch-Murnaghan phenomenological equation [58]:

$$E(V) = E_0 + \frac{9V_0B}{16}\left\{\left[\left(\frac{V_0}{V}\right)^{\frac{2}{3}} - 1\right]^3 K_P + \left[\left(\frac{V_0}{V}\right)^{\frac{2}{3}} - 1\right]^2 \times \left[6 - 4\left(\frac{V_0}{V}\right)^{\frac{2}{3}}\right]\right\}. \quad \text{(A1)}$$

In Eq. (A1) the minimum energy E_0, the equilibrium volume V_0, the 3D bulk modulus B and the parameter K_P, which has the meaning of variation of the bulk modulus with the volume, are used as fitting parameters. For the single-layer calculations, in order to use Eq. (A1), we have introduced an arbitrary width w for the materials. The optimized lattice constant was determined from the area of the 2D unit cell, obtained as V_0/w. By inspection of Eq. (A1), one can recognize that the introduction of this arbitrary width does not affect the value of the in-plane lattice constant if one shifts this dependency on the value of the 3D bulk modulus B. For this reason one can introduce a 2D bulk modulus, obtained as $B_{2D} = Bw$, whose value is also independent of the choice for the width. For the "bulk calculations," we fixed the value of the in-plane lattice constant to the one of the single layer and modified the out-of-plane lattice constant c. For this reason, the calculated bulk modulus has the correct dimensions but it refers to the out-of-plane direction only, hence we have assigned it the symbol B_z.

APPENDIX B: EFFECT OF THE SPIN ORBIT COUPLING ON THE IN-PLANE LATTICE CONSTANT

The inclusion of the SO coupling in the geometry optimizations is not customarily done. In fact, SO calculations are usually much more expensive than regular calculations, with the time and memory consumption increasing by a factor of 5–10 (or even worse) in general, depending on the system under study. Nevertheless, the effect of the SO in the final geometry could lead to non-negligible differences. In this section we repeat the analysis of the lattice constant including the SO coupling for the MoS_2 single layer, characterized by the lowest ΔSO, and the WSe_2 single layer, which is the system with the highest ΔSO for which an experimental value of the lattice constant is available. We have found that (see Fig. 15) for the LDA, the PBE, the PBE+correction, and the SCAN methods, including the SO coupling in the approach lead to the same (with a maximum difference smaller than 0.01 Å) values of the in-plane lattice constants. On the other hand, for the DF, DF2, rev-DF2, optPBE-vdW, and optB86b-vdW methods, the inclusion of the SO coupling resulted in much higher values of the lattice constant. For the dDsC and optB88-vdW none of the SO geometry optimizations converged.

APPENDIX C: NUMERICAL RESULTS

In the following, we provide the numerical data calculated in this work. The optB88-vdW calculations including the spin-orbit coupling did not converge (dnc). In each table, we also provide the corresponding experimental measurements for the given quantity, when available. In producing the figures of the main text, we reported the numerical average of the available values, whenever multiple experimental values were found for a given quantity.

1. Single layer

The relevant numerical quantities for the single layer systems are given in Tables I–VI.

2. Double layer

The relevant quantities for the double layer systems are given in Tables VII–XII. In the double-layer calculations, the in-plane lattice constant was fixed to the value obtained in the single-layer optimization. This choice entails a maximum 0.01 Å difference from the optimized double-layer values (see Appendix D).

3. Bulk

The relevant quantities for the bulk systems are given in Tables XIII–XVIII. In the bulk calculations, the in-plane lattice constant was fixed to the value obtained in the single-layer optimization. This choice entails a maximum 0.01 Å difference from the optimized bulk values (see Appendix D).

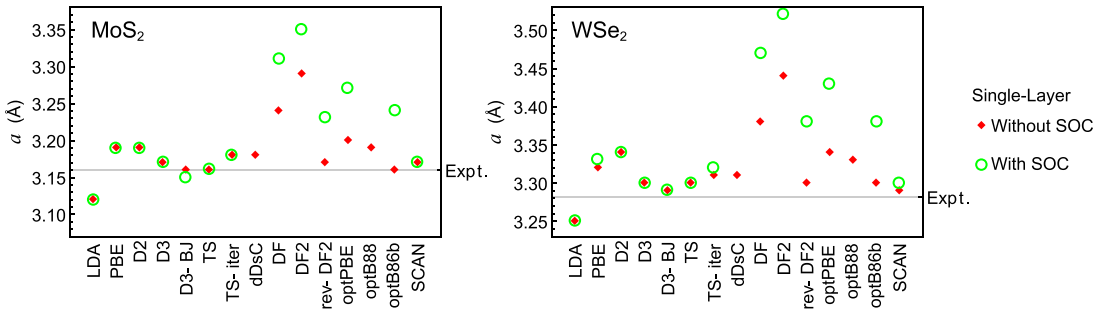

FIG. 15. In-plane lattice constant a for the single-layer MoS_2 and WSe_2 as calculated without (red diamonds) and with (green hollow circles) the spin-orbit coupling within the different modeling methods used in this work. The horizontal lines mark the experimental value of the in-plane lattice constant.

TABLE I. Results for the single-layer MoS_2 system. To obtain the 3D bulk modulus in GPa a width $w = 6.2$ Å was assumed. The direct band gap ΔE_{Dir} is realized at the K point; the indirect band gap ΔE_{Ind} is realized between the K and Γ points; the fundamental gap of the system is highlighted by bold-face characters.

	Geometry				Electronic properties		Electronic properties spin orbit		
XC	a (Å)	ΔX (Å)	B (GPa)	B_{2D} (N/m)	ΔE_{Dir} (eV)	ΔE_{Ind} (eV)	ΔE_{Dir} (eV)	ΔE_{Ind} (eV)	ΔSO(meV)
LDA	3.12	3.11	145	90.0	**1.87**	1.98	**1.79**	1.97	145
PBE	3.19	3.12	132	82.1	1.66	**1.62**	**1.58**	1.61	148
D2	3.19	3.12	133	82.8	1.66	**1.61**	**1.58**	1.60	148
D3	3.17	3.13	134	83.2	**1.73**	1.76	**1.65**	1.75	147
D3-BJ	3.16	3.13	137	85.1	**1.76**	1.82	**1.68**	1.81	146
TS	3.16	3.14	132	81.9	**1.76**	1.84	**1.69**	1.83	146
TS-iter	3.18	3.12	125	77.5	1.69	**1.68**	**1.61**	1.68	148
dDsC	3.18	3.12	135	83.4	1.69	**1.67**	**1.61**	1.66	148
DF	3.24	3.14	124	77.3	1.53	**1.44**	1.44	**1.41**	155
DF2	3.29	3.16	116	71.9	1.42	**1.25**	1.33	**1.23**	157
rev-DF2	3.17	3.13	137	84.8	**1.73**	1.78	**1.64**	1.75	149
optPBE	3.20	3.14	131	81.3	1.65	**1.64**	**1.56**	1.61	152
optB88	3.19	3.14	134	82.9	1.67	1.67	dnc	dnc	dnc
optB86b	3.16	3.14	138	85.3	**1.77**	1.85	**1.68**	1.83	148
SCAN	3.17	3.11	145	90.1	1.83	**1.80**	**1.75**	1.79	148
Experiments	3.160 [59]	3.172 [59]		171 [63]	1.90 [46] 1.83 [67]				146 [67]

TABLE II. Results for the single-layer $MoSe_2$ system; to obtain the 3D bulk modulus in GPa a width $w = 6.5$ Å was assumed. The direct band gap ΔE_{Dir} is realized at the K point; the indirect band gap ΔE_{Ind} is realized between the K and Γ points; the fundamental gap of the system is highlighted by bold-face characters.

	Geometry				Electronic properties		Electronic properties spin orbit		
XC	a (Å)	ΔX (Å)	B (GPa)	B_{2D} (N/m)	ΔE_{Dir} (eV)	ΔE_{Ind} (eV)	ΔE_{Dir} (eV)	ΔE_{Ind} (eV)	ΔSO (meV)
LDA	3.25	3.32	115	74.8	**1.63**	1.99	**1.52**	1.96	184
PBE	3.32	3.34	103	67.1	**1.45**	1.71	**1.34**	1.79	184
D2	3.32	3.33	111	72.2	**1.45**	1.69	**1.34**	1.66	184
D3	3.30	3.35	105	67.9	**1.51**	1.82	**1.40**	1.79	183
D3-BJ	3.29	3.35	108	70.3	**1.53**	1.87	**1.43**	1.84	183
TS	3.30	3.35	104	67.6	**1.51**	1.82	**1.40**	1.79	183
TS-iter	3.31	3.34	99	64.5	**1.48**	1.75	**1.37**	1.72	184
dDsC	3.31	3.34	105	68.4	**1.48**	1.75	**1.37**	1.72	184
DF	3.38	3.37	96	62.7	**1.31**	1.48	**1.20**	1.44	188
DF2	3.44	3.39	88	57.1	**1.20**	1.28	**1.09**	1.24	188
rev-DF2	3.30	3.35	107	69.9	**1.51**	1.83	**1.39**	1.78	185
optPBE	3.34	3.36	102	66.5	**1.41**	1.65	**1.29**	1.60	187
optB88	3.33	3.35	105	68.0	**1.43**	1.67	dnc	dnc	dnc
optB86b	3.30	3.35	108	70.4	**1.51**	1.82	**1.39**	1.90	185
SCAN	3.29	3.32	114	73.8	**1.63**	1.93	**1.52**	1.90	185
Experiments	3.299 [59]	3.338 [59]			1.59 [68] 1.76 [69]				160 [68] 230 [69]

TABLE III. Results for the single-layer $MoTe_2$ system; to obtain the 3D bulk modulus in GPa a width $w = 7.0$ Å was assumed. The direct band gap ΔE_{Dir} is realized at the K point; the indirect band gap ΔE_{Ind} is realized between the K and Γ points; the fundamental gap of the system is highlighted by bold-face characters.

	Geometry				Electronic properties		Electronic properties spin orbit		
XC	a (Å)	ΔX (Å)	B (GPa)	B_{2D} (N/m)	ΔE_{Dir} (eV)	ΔE_{Ind} (eV)	ΔE_{Dir} (eV)	ΔE_{Ind} (eV)	ΔSO (meV)
LDA	3.47	3.60	83	58.2	**1.24**	1.82	**1.10**	1.77	217
PBE	3.55	3.62	73	51.3	**1.09**	1.55	**0.96**	1.49	215
D2	3.53	3.63	78	54.4	**1.13**	1.65	**1.00**	1.59	214
D3	3.53	3.63	74	52.0	**1.13**	1.64	**1.00**	1.58	214
D3-BJ	3.51	3.63	77	54.0	**1.17**	1.73	**1.04**	1.66	214
TS	3.53	3.62	71	49.8	**1.13**	1.64	**1.00**	1.57	214
TS-iter	3.53	3.62	70	49.0	**1.13**	1.63	**1.00**	1.57	214
dDsC	3.54	3.62	75	52.4	**1.11**	1.58	**0.97**	1.52	215
DF	3.63	3.64	68	47.5	**0.95**	1.27	**0.81**	1.21	215
DF2	3.71	3.66	61	42.8	**0.84**	1.03	**0.71**	0.98	210
rev-DF2	3.53	3.63	77	54.0	**1.13**	1.64	**0.99**	1.57	216
optPBE	3.58	3.63	73	51.0	**1.03**	1.44	**0.89**	1.38	216
optB88	3.57	3.62	75	52.5	**1.05**	1.45	dnc	dnc	dnc
optB86b	3.53	3.63	78	54.5	**1.13**	1.63	**0.99**	1.55	216
SCAN	3.50	3.60	79	55.3	**1.29**	1.93	**1.14**	1.85	221
Experiments	3.522 [59] 3.519 [60]	3.604 [59]			1.10 [70]				250 [70]

TABLE IV. Results for the single-layer WS_2 system; to obtain the 3D bulk modulus in GPa a width $w = 6.2$ Å was assumed. The direct band gap ΔE_{Dir} is realized at the K point; the indirect band gap ΔE_{Ind} is realized between the K and Γ points; the fundamental gap of the system is highlighted by bold-face characters.

	Geometry				Electronic properties		Electronic properties spin orbit		
XC	a (Å)	ΔX (Å)	B (GPa)	B_{2D} (N/m)	ΔE_{Dir} (eV)	ΔE_{Ind} (eV)	ΔE_{Dir} (eV)	ΔE_{Ind} (eV)	ΔSO (meV)
LDA	3.13	3.12	156	95.8	**1.98**	2.13	**1.71**	2.05	421
PBE	3.19	3.14	143	88.4	**1.80**	1.84	**1.53**	1.77	432
D2	3.19	3.13	125	77.5	**1.79**	1.81	**1.53**	1.74	433
D3	3.18	3.15	143	88.4	**1.84**	1.91	**1.57**	1.84	429
D3-BJ	3.16	3.15	148	91.6	**1.92**	2.06	**1.65**	1.98	423
TS	3.17	3.15	143	88.6	**1.88**	1.99	**1.61**	1.91	426
TS-iter	3.18	3.14	139	85.9	**1.84**	1.91	**1.57**	1.83	429
dDsC	3.18	3.14	148	91.5	**1.84**	1.89	**1.57**	1.82	430
DF	3.23	3.17	135	83.8	1.71	**1.70**	**1.42**	1.63	458
DF2	3.28	3.18	125	77.7	1.59	**1.48**	**1.30**	1.40	468
rev-DF2	3.17	3.15	147	91.2	**1.89**	2.00	**1.60**	1.91	436
optPBE	3.20	3.16	142	87.8	**1.79**	1.85	**1.51**	1.76	448
optB88	3.19	3.16	144	89.1	**1.82**	1.88	dnc	dnc	dnc
optB86b	3.17	3.15	148	91.8	**1.89**	2.00	**1.60**	1.91	436
SCAN	3.16	3.12	157	97.5	**1.93**	2.02	**1.67**	1.95	429
Experiments	3.16 [44] 3.1532 [61]	3.15 [44] 3.14 [61]		177 [63]	1.98 [71]				420 [71]

TABLE V. Results for the single-layer WSe_2 system; to obtain the 3D bulk modulus in GPa a width $w = 6.6$ Å was assumed. The direct band gap ΔE_{Dir} is realized at the K point; the indirect band gap ΔE_{Ind} is realized between the K and Γ points; the fundamental gap of the system is highlighted by bold-face characters.

	Geometry				Electronic properties		Electronic properties spin orbit		
XC	a (Å)	ΔX (Å)	B (GPa)	B_{2D} (N/m)	ΔE_{Dir} (eV)	ΔE_{Ind} (eV)	ΔE_{Dir} (eV)	ΔE_{Ind} (eV)	ΔSO (meV)
LDA	3.25	3.34	127	78.7	**1.75**	2.20	**1.45**	2.04	455
PBE	3.32	3.36	115	71.3	**1.55**	1.88	**1.26**	1.75	467
D2	3.34	3.34	103	63.6	**1.47**	1.71	**1.18**	1.60	473
D3	3.30	3.37	118	72.8	**1.63**	2.01	**1.33**	1.87	461
D3-BJ	3.29	3.37	120	74.5	**1.66**	2.07	**1.36**	1.93	458
TS	3.30	3.37	116	71.9	**1.62**	2.01	**1.32**	1.87	461
TS-iter	3.31	3.36	110	68.2	**1.59**	1.93	**1.29**	1.80	464
dDsC	3.31	3.36	111	73.5	**1.58**	1.93	**1.29**	1.80	465
DF	3.38	3.38	108	66.8	**1.40**	1.63	**1.09**	1.50	495
DF2	3.44	3.40	97	60.4	**1.28**	1.41	**0.97**	1.29	502
rev-DF2	3.30	3.37	120	74.1	**1.62**	2.01	**1.31**	1.86	471
optPBE	3.34	3.38	114	70.7	**1.51**	1.81	**1.19**	1.68	484
optB88	3.33	3.37	116	72.1	**1.53**	1.83	dnc	dnc	dnc
optB86b	3.30	3.37	120	74.6	**1.62**	2.01	**1.31**	1.86	472
SCAN	3.29	3.33	127	78.8	**1.66**	2.04	**1.37**	1.92	467
Experiments	3.282 [61]	3.34 [61]			1.67 [71]				400 [71]
					1.70 [69]				480 [69]

TABLE VI. Results for the single-layer WTe_2 system; to obtain the 3D bulk modulus in GPa a width $w = 7.1$ Å was assumed. The direct band gap ΔE_{Dir} is realized at the K point; the indirect band gap ΔE_{Ind} is realized between the K and Γ points; the fundamental gap of the system is highlighted by bold-face characters.

	Geometry				Electronic properties		Electronic properties spin orbit		
XC	a (Å)	ΔX (Å)	B (GPa)	B_{2D} (N/m)	ΔE_{Dir} (eV)	ΔE_{Ind} (eV)	ΔE_{Dir} (eV)	ΔE_{Ind} (eV)	ΔSO (meV)
LDA	3.47	3.61	83	59.0	**1.26**	1.92	**0.93**	1.65	473
PBE	3.56	3.63	74	52.4	**1.13**	1.71	**0.81**	1.48	481
D2	3.56	3.62	86	61.0	**1.05**	1.53	**0.73**	1.34	488
D3	3.52	3.65	75	53.6	**1.17**	1.78	**0.84**	1.54	478
D3-BJ	3.51	3.65	77	55.1	**1.20**	1.83	**0.87**	1.57	476
TS	3.53	3.64	72	51.0	**1.13**	1.71	**0.81**	1.48	481
TS-iter	3.54	3.63	71	50.3	**1.10**	1.65	**0.78**	1.43	483
dDsC	3.54	3.63	76	53.9	**1.10**	1.65	**0.78**	1.44	484
DF	3.63	3.64	69	48.8	**0.92**	1.30	**0.59**	1.13	515
DF2	3.71	3.66	61	43.5	**0.80**	1.04	**0.47**	0.89	519
rev-DF2	3.53	3.64	78	55.2	**1.13**	1.71	**0.80**	1.47	492
optPBE	3.58	3.64	74	52.2	**1.02**	1.49	**0.69**	1.30	505
optB88	3.57	3.64	76	53.7	**1.03**	1.51	dnc	dnc	dnc
optB86b	3.53	3.64	78	55.7	**1.13**	1.70	**0.80**	1.47	492
SCAN	3.50	3.60	80.0	56.7	**1.25**	1.96	**0.92**	1.72	483

TABLE VII. Results for the double-layer MoS_2 system. The direct band gap ΔE_{Dir} is realized at the K point; when it is not specified, the indirect band gap ΔE_{Ind} is realized between the K and Γ points. The fundamental gap of the system is highlighted by bold-face characters. The interlayer interaction $I - I$ is the band splitting of the HVB at the K point without the SO interaction.

	Geometry			Electronic properties			Electronic properties spin orbit		
XC	ΔM (Å)	ΔX (Å)	ΔL (Å)	ΔE_{Dir} (eV)	ΔE_{Ind} (eV)	$I - I$ (meV)	ΔE_{Dir} (eV)	ΔE_{Ind} (eV)	ΔSO (meV)
LDA	6.05	3.11	2.94	1.83	**1.21** (T-Γ)	111	1.79	**1.20**	182
PBE	7.15	3.12	4.03	1.65	**1.47**	15	1.58	**1.47**	149
D2	6.20	3.11	3.09	1.62	**1.15**	72	1.57	**1.15**	166
D3	6.20	3.13	3.07	1.69	**1.28**	76	1.64	**1.27**	165
D3-BJ	6.07	3.13	2.94	1.72	**1.22** (T-Γ)	97	1.67	**1.21**	175
TS	6.11	3.13	2.98	1.72	**1.17**	89	1.68	**1.16**	171
TS-iter	6.12	3.12	3.00	1.65	**1.16**	84	1.61	**1.16**	169
dDsC	6.27	3.12	3.15	1.66	**1.25**	66	1.61	**1.24**	162
DF	6.56	3.15	3.42	1.52	**1.16**	37	1.44	**1.16**	158
DF2	6.44	3.16	3.28	1.41	**0.94**	44	1.33	**0.94**	165
rev-DF2	6.20	3.14	3.06	1.70	**1.28** (T-Γ)	81	**1.64**	1.30	166
optPBE	6.35	3.14	3.20	1.62	**1.25**	58	1.55	**1.26**	160
optB88	6.23	3.14	3.09	1.64	**1.23**	72	dnc	dnc	dnc
optB86b	6.20	3.14	3.06	1.73	**1.31** (T-Γ)	82	1.67	**1.34**	165
SCAN	6.20	3.11	3.09	1.79	**1.32**	77	1.74	**1.32**	167
Experiments				1.88 [46] 1.85 [67]	**1.59** [46]				155 [46]

TABLE VIII. Results for the double-layer $MoSe_2$ system. The direct band gap ΔE_{Dir} is realized at the K point; when it is not specified, the indirect band gap ΔE_{Ind} is realized between the K and Γ points. The fundamental gap of the system is highlighted by bold-face characters. The interlayer interaction, $I - I$ is the band splitting of the HVB at the K point without the SO interaction.

	Geometry			Electronic properties			Electronic properties spin orbit		
XC	ΔM (Å)	ΔX (Å)	ΔL (Å)	ΔE_{Dir} (eV)	ΔE_{Ind} (eV)	$I - I$ (meV)	ΔE_{Dir} (eV)	ΔE_{Ind} (eV)	ΔSO (meV)
LDA	6.38	3.32	3.06	1.58	**1.13** (T-Γ)	127	1.51	**1.12** (T-Γ)	222
PBE	7.14	3.34	3.80	1.44	**1.47** (T-K)	35	**1.34**	1.39 (T-K)	187
D2	6.54	3.34	3.20	1.41	**1.20** (T-Γ)	88	1.34	**1.20** (T-Γ)	203
D3	6.54	3.35	3.20	1.47	**1.22** (T-Γ)	92	1.40	**1.22** (T-Γ)	204
D3-BJ	6.39	3.35	3.04	1.49	**1.12** (T-Γ)	118	1.42	**1.11** (T-Γ)	216
TS	6.41	3.34	3.07	1.46	**1.12** (T-Γ)	110	1.39	**1.12** (T-Γ)	213
TS-iter	6.41	3.34	3.07	1.43	**1.11** (T-Γ)	108	1.36	**1.10** (T-Γ)	212
dDsC	6.60	3.34	3.26	1.44	**1.26** (T-Γ)	82	1.37	**1.25** (T-Γ)	201
DF	6.94	3.37	3.57	1.30	**1.21**	43	1.20	**1.19**	192
DF2	6.85	3.40	3.45	1.18	**0.99**	49	1.09	**0.97**	192
rev-DF2	6.52	3.35	3.16	1.47	**1.18** (T-Γ)	100	1.39	**1.22** (T-Γ)	205
optPBE	6.69	3.36	3.33	1.39	**1.26**	69	1.29	**1.25**	196
optB88	6.60	3.36	3.24	1.39	**1.21** (T-Γ)	81	dnc	dnc	dnc
optB86b	6.55	3.35	3.19	1.47	**1.21** (T-Γ)	95	1.39	**1.25** (T-Γ)	207
SCAN	6.60	3.32	3.27	1.59	**1.43** (T-Γ)	85	1.52	**1.43**	204

TABLE IX. Results for the double-layer $MoTe_2$ system. The direct band gap ΔE_{Dir} is realized at the K point; when it is not specified, the indirect band gap ΔE_{Ind} is realized between the K and Γ points. The fundamental gap of the system is highlighted by bold-face characters. The interlayer interaction $I - I$ is the band splitting of the HVB at the K point without the SO interaction.

	Geometry			Electronic properties			Electronic properties spin orbit		
XC	ΔM (Å)	ΔX (Å)	ΔL (Å)	ΔE_{Dir} (eV)	ΔE_{Ind} (eV)	$I - I$ (meV)	ΔE_{Dir} (eV)	ΔE_{Ind} (eV)	ΔSO (meV)
LDA	6.89	3.60	3.29	1.18	**1.00** (T-Γ)	154	1.10	**1.00** (T-Γ)	262
PBE	7.47	3.62	3.85	**1.06**	1.14 (T-Γ)	62	**0.96**	1.06 (T-Γ)	222
D2	7.00	3.63	3.37	1.09	**1.03** (T-Γ)	124	**1.00**	**1.00** (T-Γ)	245
D3	7.00	3.62	3.38	1.08	**1.03** (T-Γ)	122	**1.00**	1.01	244
D3-BJ	6.87	3.63	3.24	1.12	**0.92** (T-Γ)	154	1.04	**0.92** (T-Γ)	259
TS	7.00	3.62	3.38	1.08	**1.03**	120	**0.96**	1.00	243
TS-iter	7.00	3.62	3.38	1.08	**1.03**	121	**0.96**	1.00	244
dDsC	7.03	3.62	3.41	1.06	**1.02**	115	**0.96**	0.99	241
DF	7.51	3.64	3.87	**0.93**	0.99	48	**0.81**	0.97	219
DF2	7.50	3.66	3.84	0.82	**0.76**	45	**0.71**	0.74	214
rev-DF2	7.01	3.63	3.37	1.08	**1.02** (T-Γ)	125	**0.99**	1.01 (T-Γ)	240
optPBE	7.25	3.63	3.62	**1.00**	1.04	78	**0.90**	1.02	225
optB88	7.12	3.63	3.49	1.01	**0.97**	95	dnc	dnc	dnc
optB86b	7.01	3.63	3.37	1.08	**1.03** (T-Γ)	123	**0.99**	1.02 (T-Γ)	240
SCAN	7.13	3.60	3.52	1.25	**1.19** (T-Γ)	113	1.15	**1.12** (T-Γ)	245

TABLE X. Results for the double-layer WS_2 system. The direct band gap ΔE_{Dir} is realized at the K point; when it is not specified, the indirect band gap ΔE_{Ind} is realized between the K and Γ points. The fundamental gap of the system is highlighted by bold-face characters. The interlayer interaction $I - I$ is the band splitting of the HVB at the K point without the SO interaction.

	Geometry			Electronic properties			Electronic properties spin orbit		
XC	ΔM (Å)	ΔX (Å)	ΔL (Å)	ΔE_{Dir} (eV)	ΔE_{Ind} (eV)	$I - I$ (meV)	ΔE_{Dir} (eV)	ΔE_{Ind} (eV)	ΔSO (meV)
LDA	6.10	3.12	2.97	1.94	**1.35** (T-Γ)	125	1.71	**1.29** (T-Γ)	437
PBE	6.97	3.14	3.83	1.79	**1.64**	27	**1.53**	1.57	433
D2	6.11	3.13	2.98	1.75	**1.30**	105	1.52	**1.24**	444
D3	6.23	3.14	3.09	1.80	**1.44** (T-Γ)	90	1.57	**1.37**	437
D3-BJ	6.10	3.15	2.96	1.87	**1.37** (T-Γ)	116	1.65	**1.31** (T-Γ)	437
TS	6.20	3.15	3.05	1.84	**1.43** (T-Γ)	97	1.61	**1.36** (T-Γ)	436
TS-iter	6.20	3.14	3.06	1.80	**1.42** (T-Γ)	95	1.57	**1.35** (T-Γ)	438
dDsC	6.32	3.14	3.18	1.80	**1.49**	78	1.56	**1.42**	436
DF	6.62	3.17	3.45	1.69	**1.43**	45	1.42	**1.38**	459
DF2	6.45	3.18	3.27	1.57	**1.17**	56	1.30	**1.12**	472
rev-DF2	6.20	3.15	3.06	1.85	**1.40** (T-Γ)	103	1.60	**1.38** (T-Γ)	444
optPBE	6.37	3.16	3.21	1.77	**1.47**	71	1.51	**1.42**	451
optB88	6.25	3.16	3.09	1.79	**1.42** (T-Γ)	88	dnc	dnc	dnc
optB86b	6.20	3.15	3.05	1.85	**1.42** (T-Γ)	101	1.61	**1.39**	445
SCAN	6.24	3.12	3.12	1.89	**1.57**	91	1.67	**1.51**	440
Experiments					1.94 [71]				420 [71]

TABLE XI. Results for the double-layer WSe_2 system. The direct band gap ΔE_{Dir} is realized at the K point; when it is not specified, the indirect band gap ΔE_{Ind} is realized between the K and Γ points. The fundamental gap of the system is highlighted by bold-face characters. The interlayer interaction $I - I$ is the band splitting of the HVB at the K point without the SO interaction.

	Geometry			Electronic properties			Electronic properties spin orbit		
XC	ΔM (Å)	ΔX (Å)	ΔL (Å)	ΔE_{Dir} (eV)	ΔE_{Ind} (eV)	$I - I$ (meV)	ΔE_{Dir} (eV)	ΔE_{Ind} (eV)	ΔSO (meV)
LDA	6.41	3.34	3.06	1.69	**1.28** (T-Γ)	153	1.45	**1.19** (T-K)	476
PBE	7.22	3.36	3.85	1.54	**1.52** (T-K)	41	1.26	**1.25** (T-K)	468
D2	6.42	3.33	3.09	1.42	**1.21**	123	1.18	**1.11**	487
D3	6.55	3.37	3.18	1.57	**1.37** (T-Γ)	116	1.32	**1.19** (T-K)	473
D3-BJ	6.42	3.37	3.05	1.60	**1.28** (T-Γ)	144	1.36	**1.17** (T-K)	477
TS	6.60	3.37	3.23	1.58	**1.40** (T-Γ)	108	1.32	**1.19** (T-K)	472
TS-iter	6.53	3.36	3.17	1.54	**1.35** (T-Γ)	116	1.29	**1.20** (T-K)	476
dDsC	6.60	3.36	3.25	1.54	**1.39** (T-Γ)	104	1.29	**1.21** (T-K)	474
DF	6.98	3.38	3.60	1.38	**1.37**	52	**1.09**	1.21 (T-K)	497
DF2	6.88	3.41	3.47	1.27	**1.13**	60	**0.96**	1.04	509
rev-DF2	6.55	3.37	3.17	1.56	**1.33** (T-Γ)	122	1.31	**1.18** (T-K)	481
optPBE	6.73	3.38	3.35	1.47	**1.42** (T-Γ)	84	**1.20**	**1.20** (T-K)	488
optB88	6.60	3.37	3.23	1.49	**1.34** (T-Γ)	102	dnc	dnc	dnc
optB86b	6.60	3.37	3.22	1.58	**1.38** (T-Γ)	111	1.31	**1.19** (T-K)	480
SCAN	6.60	3.33	3.27	1.62	**1.59** (T-Γ)	105	**1.33**	1.36 (T-K)	514
Experiments					1.61 [71]				400 [71]

TABLE XII. Results for the double-layer WTe_2 system. The direct band gap ΔE_{Dir} is realized at the K point; when it is not specified, the indirect band gap ΔE_{Ind} is realized between the K and Γ points. The fundamental gap of the system is highlighted by bold-face characters. The interlayer interaction $I - I$ is the band splitting of the HVB at the K point without the SO interaction.

	Geometry			Electronic properties			Electronic properties spin orbit		
XC	ΔM (Å)	ΔX (Å)	ΔL (Å)	ΔE_{Dir} (eV)	ΔE_{Ind} (eV)	$I - I$ (meV)	ΔE_{Dir} (eV)	ΔE_{Ind} (eV)	ΔSO (meV)
LDA	6.93	3.62	3.30	1.19	**1.11** (T-K)	184	**0.93**	0.94 (T-K)	500
PBE	7.49	3.63	3.86	**1.02**	1.19 (T-K)	75	**0.74**	0.96 (T-K)	492
D2	6.92	3.62	3.31	0.98	**0.93**	159	**0.73**	0.79	508
D3	7.00	3.65	3.35	1.11	**1.09** (T-K)	160	**0.84**	0.91 (T-K)	498
D3-BJ	6.87	3.65	3.22	1.12	**1.06** (T-K)	195	**0.87**	0.90 (T-K)	506
TS	7.09	3.64	3.45	**1.08**	1.12 (T-K)	137	**0.81**	0.93 (T-K)	496
TS-iter	7.00	3.63	3.37	**1.04**	1.08	150	**0.78**	0.93	501
dDsC	7.04	3.63	3.41	**1.05**	1.12 (T-K)	148	**0.79**	0.93 (T-K)	500
DF	7.49	3.64	3.84	**0.90**	1.03	64	**0.59**	0.90	517
DF2	7.44	3.66	3.77	0.78	**0.77**	62	**0.47**	0.65	521
rev-DF2	7.04	3.65	3.39	**1.08**	1.09 (T-K)	152	**0.80**	0.91	507
optPBE	7.25	3.64	3.61	**0.98**	1.11	100	**0.69**	0.93	510
optB88	7.14	3.64	3.50	**0.99**	1.06	117	dnc	dnc	dnc
optB86b	7.03	3.65	3.38	**1.08**	1.10 (T-K)	152	**0.80**	0.92 (T-K)	506
SCAN	7.14	3.61	3.53	**1.19**	1.24 (T-K)	138	**0.92**	1.05 (T-K)	500

TABLE XIII. Results for the bulk MoS_2. ΔE_{Dir} is the minimum vertical distance between HVB and LCB; ΔE_{Fund} is obtained as Max[HVB]-Min[LCB].

	Geometry				Electronic properties		Electronic properties spin orbit	
XC	c (Å)	ΔX (Å)	ΔL (Å)	B_z(GPa)	ΔE_{Dir} (eV)	ΔE_{Fund} (eV)	ΔE_{Dir} (eV)	ΔE_{Fund} (eV)
LDA	12.12	3.11	2.95	54	1.78	0.76	1.75	0.76
PBE	14.78	3.12	4.27	1.8	1.65	1.42	1.58	1.41
D2	12.44	3.11	3.11	48	1.59	0.93	1.56	0.93
D3	12.34	3.12	3.05	48	1.65	0.90	1.62	0.90
D3-BJ	12.10	3.12	2.93	61	1.67	0.80	1.64	0.79
TS	12.06	3.12	2.91	51	1.67	0.78	1.64	0.77
TS-iter	12.06	3.11	2.92	44	1.60	0.77	1.57	0.77
dDsC	12.74	3.12	3.25	34	1.64	1.06	1.60	1.05
DF	13.14	3.15	3.42	28	1.50	1.00	1.44	1.01
DF2	12.88	3.16	3.28	41	1.39	0.78	1.33	0.79
rev-DF2	12.36	3.13	3.05	49	1.66	0.87	1.62	0.94
optPBE	12.76	3.14	3.24	38	1.60	1.04	1.55	1.09
optB88	12.50	3.14	3.11	48	1.61	0.93	dnc	dnc
optB86b	12.40	3.14	3.06	48	1.70	0.92	1.66	0.98
SCAN	12.50	3.11	3.14	46	1.76	1.08	1.72	1.09
Experiments	12.294 [59]	3.172 [59]	2.975 [59]		1.74 [43] 1.910 [44] 1.88 [45]	1.23 [43] 1.23 [43]		

TABLE XIV. Results for the bulk $MoSe_2$. ΔE_{Dir} is the minimum vertical distance between HVB and LCB; ΔE_{Fund} is obtained as Max[HVB]-Min[LCB].

	Geometry				Electronic properties		Electronic properties spin orbit	
XC	c (Å)	ΔX (Å)	ΔL (Å)	B_z (GPa)	ΔE_{Dir} (eV)	ΔE_{Fund} (eV)	ΔE_{Dir} (eV)	ΔE_{Fund} (eV)
LDA	12.78	3.32	3.07	50	1.52	0.76	1.48	0.75
PBE	15.26	3.34	4.29	1.9	1.44	1.43	1.34	1.34
D2	13.04	3.33	3.19	65	1.37	0.87	1.31	0.86
D3	13.02	3.34	3.17	45	1.42	0.87	1.37	0.86
D3-BJ	12.74	3.34	3.03	62	1.43	0.76	1.38	0.75
TS	12.78	3.34	3.05	39	1.40	0.78	1.35	0.77
TS-iter	12.70	3.33	3.02	44	1.37	0.74	1.32	0.73
dDsC	13.42	3.34	3.37	27	1.41	1.01	1.35	1.00
DF	13.90	3.37	3.58	26	1.28	1.08	1.19	1.07
DF2	13.70	3.39	3.46	35	1.16	0.87	1.08	0.86
rev-DF2	13.06	3.36	3.17	49	1.43	0.85	1.36	0.91
optPBE	13.46	3.36	3.37	36	1.35	0.99	1.28	1.04
optB88	13.20	3.36	3.24	46	1.36	0.89	dnc	dnc
optB86b	13.08	3.36	3.18	48	1.43	0.87	1.37	0.93
SCAN	13.20	3.33	3.27	45	1.56	1.08	1.50	1.08
Experiments	12.938 [59]	3.338 [59]	3.131 [59]		1.38 [43] 1.598 [44] 1.57 [45]	1.09 [43]		

TABLE XV. Results for the bulk $MoTe_2$. ΔE_{Dir} is the minimum vertical distance between HVB and LCB; ΔE_{Fund} is obtained as Max[HVB]-Min[LCB].

	Geometry				Electronic properties		Electronic properties spin orbit	
XC	c (Å)	ΔX (Å)	ΔL (Å)	B_z (GPa)	ΔE_{Dir} (eV)	ΔE_{Fund} (eV)	ΔE_{Dir} (eV)	ΔE_{Fund} (eV)
LDA	13.80	3.60	3.30	53	1.12	0.66	1.03	0.65
PBE	15.34	3.62	4.05	4.1	1.05	0.97	0.95	0.90
D2	13.98	3.63	3.36	83	1.03	0.70	0.96	0.69
D3	14.04	3.62	3.40	38	1.03	0.73	0.96	0.71
D3-BJ	13.68	3.63	3.21	66	1.04	0.59	0.97	0.58
TS	14.00	3.61	3.39	31	1.02	0.72	0.96	0.70
TS-iter	13.88	3.61	3.33	30	1.02	0.67	0.95	0.65
dDsC	14.36	3.62	3.56	32	1.02	0.84	0.95	0.79
DF	15.04	3.64	3.88	22	0.91	0.90	0.81	0.81
DF2	14.92	3.66	3.80	30	0.80	0.67	0.71	0.65
rev-DF2	14.10	3.65	3.40	46	1.04	0.73	0.96	0.77
optPBE	14.52	3.64	3.62	32	0.97	0.85	0.88	0.85
optB88	14.26	3.63	3.50	42	0.97	0.77	dnc	dnc
optB86b	14.10	3.63	3.42	46	1.04	0.74	0.96	0.77
SCAN	14.30	3.61	3.54	40	1.20	0.89	1.12	0.85
Experiments	13.968 [59] 13.964 [60]	3.604 [59]	3.380 [59]		1.120 [44] 1.10 [45] 1.02 [47]	0.88 [47]		

TABLE XVI. Results for the bulk WS_2. ΔE_{Dir} is the minimum vertical distance between HVB and LCB; ΔE_{Fund} is obtained as Max[HVB]-Min[LCB].

	Geometry				Electronic properties		Electronic properties spin orbit	
XC	c (Å)	ΔX (Å)	ΔL (Å)	B_z (GPa)	ΔE_{Dir} (eV)	ΔE_{Fund} (eV)	ΔE_{Dir} (eV)	ΔE_{Fund} (eV)
LDA	12.18	3.13	2.96	52	1.88	0.86	1.68	0.82
PBE	14.82	3.14	4.27	1.7	1.79	1.62	1.53	1.53
D2	12.16	3.12	2.96	65	1.69	0.91	1.50	0.87
D3	12.44	3.14	3.08	50	1.75	1.03	1.55	0.98
D3-BJ	12.16	3.15	2.93	65	1.81	0.91	1.62	0.87
TS	12.26	3.14	2.99	40	1.78	0.95	1.58	0.91
TS-iter	12.18	3.14	2.95	51	1.74	0.92	1.54	0.88
dDsC	12.80	3.14	3.26	33	1.77	1.16	1.55	1.11
DF	13.20	3.17	3.43	30	1.67	1.25	1.42	1.21
DF2	12.96	3.18	3.30	41	1.54	1.01	1.30	0.98
rev-DF2	12.44	3.16	3.06	50	1.81	0.99	1.59	1.02
optPBE	12.82	3.16	3.25	38	1.74	1.15	1.51	1.16
optB88	12.56	3.16	3.12	46	1.75	1.04	dnc	dnc
optB86b	12.48	3.16	3.08	49	1.81	1.02	1.59	1.04
SCAN	12.56	3.12	3.16	44	1.86	1.21	1.66	1.18
Experiments	12.323 [61]	3.14 [61]	3.02 [61]		1.79 [43]	1.35 [43]		

TABLE XVII. Results for the bulk WSe_2. ΔE_{Dir} is the minimum vertical distance between HVB and LCB; ΔE_{Fund} is obtained as Max[HVB]-Min[LCB].

	Geometry				Electronic properties		Electronic properties spin orbit	
XC	c (Å)	ΔX (Å)	ΔL (Å)	B_z (GPa)	ΔE_{Dir} (eV)	ΔE_{Fund} (eV)	ΔE_{Dir} (eV)	ΔE_{Fund} (eV)
LDA	12.86	3.34	3.09	53	1.63	0.89	1.39	0.82
PBE	15.36	3.36	4.32	1.5	1.54	1.47	1.26	1.21
D2	12.78	3.33	3.06	72	1.35	0.89	1.14	0.83
D3	13.02	3.36	3.15	50	1.51	0.97	1.29	0.91
D3-BJ	12.80	3.37	3.03	65	1.53	0.89	1.30	0.82
TS	12.98	3.36	3.13	36	1.51	0.96	1.28	0.89
TS-iter	12.86	3.36	3.07	48	1.46	0.91	1.26	0.85
dDsC	12.50	3.36	2.89	33	1.51	1.14	1.27	1.06
DF	13.94	3.38	3.59	26	1.36	1.21	1.09	1.09
DF2	13.74	3.41	3.46	37	1.23	1.01	0.96	0.92
rev-DF2	13.12	3.38	3.18	47	1.53	0.97	1.29	0.97
optPBE	13.52	3.38	3.38	36	1.44	1.11	1.19	1.07
optB88	13.26	3.38	3.25	45	1.45	1.02	dnc	dnc
optB86b	13.14	3.38	3.19	46	1.53	0.99	1.29	0.99
SCAN	13.24	3.33	3.29	44	1.58	1.22	1.36	1.17
Experiments	12.96 [61]	3.34 [61]	3.14 [61]		1.39 [43] 1.694 [44] 1.71 [45]	1.20 [43]		

TABLE XVIII. Results for the bulk WTe_2. ΔE_{Dir} is the minimum vertical distance between HVB and LCB; ΔE_{Fund} is obtained as Max[HVB]-Min[LCB].

	Geometry				Electronic properties		Electronic properties spin orbit	
XC	c (Å)	ΔX (Å)	ΔL (Å)	B_z (GPa)	ΔE_{Dir} (eV)	ΔE_{Fund} (eV)	ΔE_{Dir} (eV)	ΔE_{Fund} (eV)
LDA	13.86	3.62	3.31	52	1.12	0.76	0.83	0.61
PBE	15.44	3.63	4.09	3.8	1.01	1.01	0.73	0.73
D2	13.82	3.62	3.29	83	0.93	0.75	0.70	0.64
D3	14.04	3.64	3.38	41	1.04	0.79	0.78	0.63
D3-BJ	13.74	3.65	3.22	69	1.04	0.73	0.76	0.59
TS	14.16	3.63	3.45	33	1.01	0.83	0.76	0.66
TS-iter	13.98	3.62	3.37	29	0.97	0.82	0.73	0.65
dDsC	14.42	3.64	3.57	33	1.01	0.87	0.76	0.68
DF	15.06	3.65	3.88	22	0.87	0.87	0.59	0.59
DF2	14.92	3.66	3.80	31	0.75	0.69	0.47	0.47
rev-DF2	14.14	3.65	3.42	48	1.02	0.80	0.76	0.66
optPBE	14.56	3.65	3.63	32	0.94	0.91	0.68	0.68
optB88	14.30	3.64	3.51	43	0.94	0.87	dnc	dnc
optB86b	14.14	3.65	3.42	47	1.02	0.81	0.76	0.66
SCAN	14.30	3.61	3.54	42	1.14	0.93	0.89	0.77

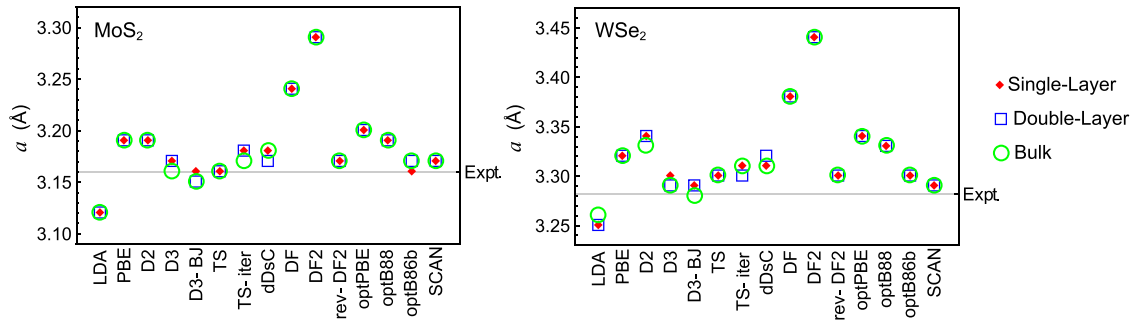

FIG. 16. In-plane lattice constant a for MoS_2 and WSe_2 in the single-layer (red diamonds), double-layer (blue squares), and bulk (green circles) systems, as obtained with the different modeling methods used in this work. The horizontal lines mark the experimental value of the in-plane lattice constant of single-layer systems.

APPENDIX D: IN-PLANE LATTICE CONSTANT OF THE SINGLE-LAYER, DOUBLE-LAYER, AND BULK SYSTEMS

It is not obvious that the value of the in-plane lattice constant does not depend on the number of layers, even in the case of weakly interacting layered materials. In our analysis we have set the in-plane lattice constant of the double layer and the bulk materials to be equal to the one of the single layer for two main reasons: (1) to see the effect of changing one parameter at a time (the interlayer distance in the double-layer and the out-of-plane lattice constant in the bulk material); (2) to mimic what it is "customarily" done in creating an interface between 2D materials (in general one calculates the in-plane lattice constants of both materials and then constructs an interface with a matched lattice constant, which should minimize the differences between the lattice constant of the constituent materials, while also taking into account the stiffness of each material). To understand the effects of our particular choice, in Fig. 16 we report a comparison of the optimal in-plane lattice constants for the single-layer, double-layer, and the bulk MoS_2 and WSe_2, resulting from the different methods employed in our work. The optimal values of the in-plane lattice constants for single-layer, double-layer, and bulk (within a single method) differ by a maximum value of 0.01 Å, hence adopting the value of the in-plane lattice constant of the single-layer in the double-layer or bulk calculations entails a 0.01 Å "maximum error."

[1] K. S. Novoselov, A. K. Geim, S. V. Morozov, D. Jiang, Y. Zhang, S. V. Dubonos, I. V. Grigorieva, and A. A. Firsov, Science **306**, 666 (2004).

[2] N. Mounet, M. Gibertini, P. Schwaller, D. Campi, A. Merkys, A. Marrazzo, T. Sohier, I. E. Castelli, A. Cepellotti, G. Pizzi, and N. Marzari, Nat. Nanotechnol. **13**, 246 (2018).

[3] M. Ashton, J. Paul, S. B. Sinnott, and R. G. Hennig, Phys. Rev. Lett. **118**, 106101 (2017).

[4] S. Yang, P. Zhang, A. S. Nia, and X. Feng, Adv. Mater. **32**, 1907857 (2020).

[5] A. K. Geim and I. V. Grigorieva, Nature (London) **499**, 419 (2013).

[6] R. M. Martin, *Electronic Structure: Basic Theory and Practical Methods* (Cambrige University Press, Cambridge, 2004).

[7] J. Klimeš, D. R. Bowler, and A. Michaelides, Phys. Rev. B **83**, 195131 (2011).

[8] G. Román-Pérez and J. M. Soler, Phys. Rev. Lett. **103**, 096102 (2009).

[9] M. Dion, H. Rydberg, E. Schröder, D. C. Langreth, and B. I. Lundqvist, Phys. Rev. Lett. **92**, 246401 (2004).

[10] K. Lee, E. D. Murray, L. Kong, B. I. Lundqvist, and D. C. Langreth, Phys. Rev. B **82**, 081101(R) (2010).

[11] I. Hamada, Phys. Rev. B **89**, 121103(R) (2014).

[12] H. Peng, Z.-H. Yang, J. P. Perdew, and J. Sun, Phys. Rev. X **6**, 041005 (2016).

[13] S. Grimme, J. Comput. Chem. **27**, 1787 (2006).

[14] S. Grimme, J. Antony, S. Ehrlich, and H. Krieg, J. Chem. Phys. **132**, 154104 (2010).

[15] S. Grimme, S. Ehrlich, and L. Goerigk, J. Comput. Chem. **32**, 1456 (2011).

[16] A. Tkatchenko and M. Scheffler, Phys. Rev. Lett. **102**, 073005 (2009).

[17] A. Tkatchenko, R. A. DiStasio, R. Car, and M. Scheffler, Phys. Rev. Lett. **108**, 236402 (2012).

[18] T. Bučko, S. Lebègue, J. G. Ángyán, and J. Hafner, J. Chem. Phys. **141**, 034114 (2014).

[19] S. N. Steinmann and C. Corminboeuf, J. Chem. Theory Comput. **7**, 3567 (2011).

[20] S. N. Steinmann and C. Corminboeuf, J. Chem. Phys. **134**, 044117 (2011).

[21] D. Stradi, S. Barja, C. Díaz, M. Garnica, B. Borca, J. J. Hinarejos, D. Sánchez-Portal, M. Alcamí, A. Arnau, A. L. Vázquez de Parga, R. Miranda, and F. Martín, Phys. Rev. Lett. **106**, 186102 (2011).

[22] S. Koch, D. Stradi, E. Gnecco, S. Barja, S. Kawai, C. Díaz, M. Alcamí, F. Martín, A. L. Vázquez de Parga, R. Miranda, T. Glatzel, and E. Meyer, ACS Nano **7**, 2927 (2013).

[23] Y. Han, M. C. Tringides, J. W. Evans, and P. A. Thiel, Phys. Rev. Research **2**, 013182 (2020).

[24] F. Conte, D. Ninno, and G. Cantele, Phys. Rev. Research **2**, 033001 (2020).

[25] S. Park, S. Kang, H. Kim, K. H. Lee, P. Kim, S. Sim, N. Lee, B. Karuppannan, J. Kim, J. Kim, K. I. Sim, M. J. Coak, Y.

Noda, C.-H. Park, J. H. Kim, and J.-G. Park, Sci. Rep. **10**, 20998 (2020).
[26] S. W. Jang, H. Yoon, M. Y. Jeong, S. Ryee, H.-S. Kim, and M. J. Han, Nanoscale **12**, 13501 (2020).
[27] S. Manzeli, D. Ovchinnikov, D. Pasquier, O. V. Yazyev, and A. Kis, Nat. Rev. Mater. **2**, 17033 (2017).
[28] Q. H. Wang, K. Kalantar-Zadeh, A. Kis, J. N. Coleman, and M. S. Strano, Nat. Nanotechnol. **7**, 699 (2012).
[29] W. S. Yun, S. W. Han, S. C. Hong, I. G. Kim, and J. D. Lee, Phys. Rev. B **85**, 033305 (2012).
[30] E. Scalise, M. Houssa, G. Pourtois, V. Afanas'ev, and A. Stesmans, Nano Res. **5**, 43 (2012).
[31] S. Manzeli, A. Allain, A. Ghadimi, and A. Kis, Nano Lett. **15**, 5330 (2015).
[32] E. Blundo, M. Felici, T. Yildirim, G. Pettinari, D. Tedeschi, A. Miriametro, B. Liu, W. Ma, Y. Lu, and A. Polimeni, Phys. Rev. Research **2**, 012024(R) (2020).
[33] P. Gant, P. Huang, D. Pérez de Lara, D. Guo, R. Frisenda, and A. Castellanos-Gomez, Materials Today **27**, 8 (2019).
[34] X. Qian, J. Liu, L. Fu, and J. Li, Science **346**, 1344 (2014).
[35] F. Zheng, C. Cai, S. Ge, X. Zhang, X. Liu, H. Lu, Y. Zhang, J. Qiu, T. Taniguchi, K. Watanabe, S. Jia, J. Qi, J.-H. Chen, D. Sun, and J. Feng, Adv. Mater. **28**, 4845 (2016).
[36] F. A. Rasmussen and K. S. Thygesen, J. Phys. Chem. C **119**, 13169 (2015).
[37] T. Björkman, A. Gulans, A. V. Krasheninnikov, and R. M. Nieminen, Phys. Rev. Lett. **108**, 235502 (2012).
[38] T. Björkman, J. Chem. Phys. **141**, 074708 (2014).
[39] T. Björkman, A. Gulans, A. V. Krasheninnikov, and R. M. Nieminen, J. Phys.: Condens. Matter **24**, 424218 (2012).
[40] S. A. Tawfik, T. Gould, C. Stampfl, and M. J. Ford, Phys. Rev. Materials **2**, 034005 (2018).
[41] S. Haastrup, M. Strange, M. Pandey, T. Deilmann, P. S. Schmidt, N. F. Hinsche, M. N. Gjerding, D. Torelli, P. M. Larsen, A. C. Riis-Jensen, J. Gath, K. W. Jacobsen, J. J. Mortensen, T. Olsen, and K. S. Thygesen, 2D Materials **5**, 042002 (2018).
[42] J. He, K. Hummer, and C. Franchini, Phys. Rev. B **89**, 075409 (2014).
[43] K. K. Kam and B. A. Parkinson, J. Phys. Chem. **86**, 463 (1982).
[44] R. A. Bromley, R. B. Murray, and A. D. Yoffe, J. Phys. C **5**, 759 (1972).
[45] R. Coehoorn, C. Haas, and R. A. de Groot, Phys. Rev. B **35**, 6203 (1987).
[46] K. F. Mak, C. Lee, J. Hone, J. Shan, and T. F. Heinz, Phys. Rev. Lett. **105**, 136805 (2010).
[47] I. G. Lezama, A. Ubaldini, M. Longobardi, E. Giannini, C. Renner, A. B. Kuzmenko, and A. F. Morpurgo, 2D Materials **1**, 021002 (2014).
[48] J. P. Perdew, K. Burke, and M. Ernzerhof, Phys. Rev. Lett. **77**, 3865 (1996).
[49] Z. He and W. Que, Appl. Materi. Today **3**, 23 (2016).
[50] P. E. Blöchl, Phys. Rev. B **50**, 17953 (1994).
[51] G. Kresse and D. Joubert, Phys. Rev. B **59**, 1758 (1999).
[52] G. Kresse and J. Furthmüller, Comput. Mater. Sci. **6**, 15 (1996).
[53] G. Kresse and J. Furthmüller, Phys. Rev. B **54**, 11169 (1996).
[54] H. J. Monkhorst and J. D. Pack, Phys. Rev. B **13**, 5188 (1976).
[55] D. M. Ceperley and B. J. Alder, Phys. Rev. Lett. **45**, 566 (1980).
[56] J. P. Perdew and K. Burke, Int. J. Quant. Chem. **57**, 309 (1996).
[57] J. Klimeš, D. R. Bowler, and A. Michaelides, J. Phys.: Condens. Matter **22**, 022201 (2009).
[58] F. Birch, Phys. Rev. **71**, 809 (1947).
[59] T. Böker, R. Severin, A. Müller, C. Janowitz, R. Manzke, D. Voß, P. Krüger, A. Mazur, and J. Pollmann, Phys. Rev. B **64**, 235305 (2001).
[60] D. Puotinen and R. E. Newnham, Acta Crystallogr. **14**, 691 (1961).
[61] W. Schutte, J. L. De Boer, and F. Jellinek, J. Solid State Chem. **70**, 207 (1987).
[62] Y. Ding, Y. Wang, J. Ni, L. Shi, S. Shi, and W. Tang, Phys. B: Condens. Matter **406**, 2254 (2011).
[63] K. Liu, Q. Yan, M. Chen, W. Fan, Y. Sun, J. Suh, D. Fu, S. Lee, J. Zhou, S. Tongay, J. Ji, J. B. Neaton, and J. Wu, Nano Lett. **14**, 5097 (2014).
[64] B. Amorim, A. Cortijo, F. de Juan, A. G. Grushin, F. Guinea, A. Gutiérrez-Rubio, H. Ochoa, V. Parente, R. Roldán, P. San-Jose, J. Schiefele, M. Sturla, and M. Vozmediano, Phys. Rep. **617**, 1 (2016).
[65] C. Filippi, D. J. Singh, and C. J. Umrigar, Phys. Rev. B **50**, 14947 (1994).
[66] The DF and DF2 methods, however, yield wrong a $\Delta E_{\mathrm{Dir}} < \Delta E_{\mathrm{Ind}}$ result for single-layer MoS_2.
[67] A. Splendiani, L. Sun, Y. Zhang, T. Li, J. Kim, C.-Y. Chim, G. Galli, and F. Wang, Nano Lett. **10**, 1271 (2010).
[68] J. Quereda, T. S. Ghiasi, F. A. van Zwol, C. H. van der Wal, and B. J. van Wees, 2D Materials **5**, 015004 (2017).
[69] A. R. Klots, A. K. M. Newaz, B. Wang, D. Prasai, H. Krzyzanowska, J. Lin, D. Caudel, N. J. Ghimire, J. Yan, B. L. Ivanov, K. A. Velizhanin, A. Burger, D. G. Mandrus, N. H. Tolk, S. T. Pantelides, and K. I. Bolotin, Sci. Rep. **4**, 6608 (2014).
[70] C. Ruppert, O. B. Aslan, and T. F. Heinz, Nano Lett. **14**, 6231 (2014).
[71] W. Zhao, Z. Ghorannevis, L. Chu, M. Toh, C. Kloc, P.-H. Tan, and G. Eda, ACS Nano **7**, 791 (2013).
[72] J. A. Silva-Guillén, E. Canadell, F. Guinea, and R. Roldán, ACS Photonics **5**, 3231 (2018).